



# Structure matching driven by joint-saliency-structure adaptive kernel regression



Binjie Qin<sup>a,\*</sup>, Zhuangming Shen<sup>a,1</sup>, Zien Zhou<sup>b,1</sup>, Jiawei Zhou<sup>a,1</sup>, Yisong Lv<sup>c</sup>

<sup>a</sup> School of Biomedical Engineering, Shanghai Jiao Tong University, Shanghai 200240, China

<sup>b</sup> Department of Radiology, Renji Hospital, School of Medicine, Shanghai Jiao Tong University, Shanghai 200240, China

<sup>c</sup> Department of Mathematics, Shanghai Jiao Tong University, Shanghai 200240, China

## ARTICLE INFO

### Article history:

Received 16 May 2015

Received in revised form 27 August 2015

Accepted 19 October 2015

Available online 27 November 2015

### Keywords:

Local approximation

Kernel regression

Structure matching

Nonrigid registration

Outliers

Joint saliency map

## ABSTRACT

Matching outlier structures with missing correspondences and/or local large deformations is very difficult in image registration. In this paper, we define structure matching as an iterative local adaptive kernel regression which locally reconstructs moving image's dense deformation fields from the discrete displacement fields computed by multi-resolution block matching. First, a new joint saliency map (JSM) is proposed to match a structure-tensor-based local saliency distribution for each overlapping pixel pair and highlight the corresponding saliency structures (called joint saliency structures, JSSs) between the images. To explore the consistency of normal JSSs and their deformations around the outliers, we use JSM to guide the dense deformation reconstruction by emphasizing the JSSs' discrete displacement vectors in kernel regression. The JSS adaptive kernel regression adapts anisotropic kernel's shape and orientation to reference image's structure and weights more contribution from JSSs' displacement vectors for the iterative regression, whereby moving image's local deformations can be compliant with reference image's corresponding normal structures. The experimental results demonstrate that the proposed method achieves almost the best performance in structure matching of all challenging image pairs with outlier structures compared with other state-of-the-art intensity-based nonrigid registration algorithms.

© 2015 Elsevier B.V. All rights reserved.

## 1. Introduction

With various imaging sensors offering big image data, matching local structures within the image data has attracted more attention at motion tracking, visual data recognition, change detection, image segmentation, surface reconstruction in the computer vision, pattern recognition and remote sensing for the last decade. In the computer vision community, the structure matching is also known as nonrigid image registration [1] or the optical flow problem [2]. The objective of structure matching is to determine the local transformations that align every structures (or features) in moving (or source) image with the corresponding structures in the reference (or template) image. However, owing to the image content changes over a period of time and the different physical mechanisms of multimodal imaging sensors, some local structures presented in one image appear partially or even disappear completely in another image. Such local structures with missing correspondences are

closely intertwined with the structures' local large deformations in the structure matching. The missing correspondences and local large deformations of structures are called outliers in this paper. At present, it is still a challenging task for matching these outlier structures with missing correspondences and/or the local large deformations.

Over the last several decades, many relevant works were proposed to match the local structures (or features points) of the two images by minimizing the feature-based [3–9] or intensity-based differences between the two images. Feature-based approaches are local model based methods because they always use local feature detectors and descriptors (such as SIFT [2], attribute vector [9]) to select some corresponding features in the images, and then directly match the local features by finding a geometrical transformation from these feature correspondences. To tackle the outlier problem, the popular robust point matching (RPM) [3] work proposed fuzzy softassign strategy for correspondence matrix within iterative deterministic annealing to guarantee one-to-one correspondence. Recent work enforced sparsity prior in the correspondence matrix [4] or incorporated the inverse consistency constraints into the cost function of RPM [5]. Alternatively, the coherence point drift (CPD) work [6] considered the feature point matching as a probability

\* Corresponding author. Tel.: +86 2134204382.

E-mail address: [bjqin@sjtu.edu.cn](mailto:bjqin@sjtu.edu.cn) (B. Qin).

<sup>1</sup> These authors contributed equally to this work.

density estimation problem with Gaussian mixture model representing the feature points. The recent graph-based CPD work [7] explored graph centralities to bring topological information during the correspondence computation. Furthermore, feature-dependant finite mixture model was proposed in [8]. Though these algorithms are robust to the missing correspondences, due to the smooth transformation computation being very sensitive to the ambiguity in finding local feature correspondences, the joint estimation of correspondence and smooth transformation is still difficult to the outlier issues that have both missing correspondences and local large deformations.

By directly using the complete image data to recover dense correspondences at pixel-level precision, most intensity-based nonrigid registration approaches are regarded as global model based methods that are often formulated as global energy minimization problems with the energy being composed of an regularization term and a similarity term [10–14]. The relative weight of similarity term and regularization term can cause the well-known trade-off between the registration accuracy and the smoothness of the deformation field [12]. In the presence of outliers, the accurate and plausible local structure matching does not exist using whole-intensity driven transformation model. The relative spatial regularization can either cause non-smooth and implausible distortion in these outlier regions or introduce over-smooth and inaccurate mapping artifacts between the whole images. This outlier problem can be partly solved by implementing expectation and maximization algorithm to estimate the missing or partial data [10,11], using a locally varying weight between regularization and image similarity [13–18], creating artificial correspondences [19–24] and cost-function masking [25–27], or developing SIFT flow for large displacement [2]. Most of these approaches are largely dependent on outlier region segmentation without giving full consideration to both the missing correspondences and local large deformations.

At present, there is no doubt that methods and algorithms from intelligent computing and machine learning are very demanded to tackle this challenging outlier problem in structure matching. In these research fields, outliers mean the extreme observations substantially different from all other ones in the real data. In structure matching, the missing correspondences and local large deformations introduce the extreme local geometric and intensity differences between the two images to be registered. The desired structure matching methods should be able to match moving image's local structures to the corresponding reference image's structures from these various local differences. Therefore, the classical local (nonparametric) kernel regression (or local approximation) that is adept at handling the locally varying differences is necessary to account for these outliers, and it provides the rationale behind this work. By successfully handling the locally varying differences in pattern recognition and machine learning, local kernel regression [28,29] is regarded as an ideal local regression model to effectively reconstruct the desired local signal while suppressing the outlier and noise effects. The normalized convolution used by Suarez et al. [30] and the fuzzy kernel regression proposed in [31] are two typical applications of local kernel regression which estimate each pixel's dense deformation from weighted contributions of its surrounding displacement fields in a moving isotropic window/kernel. Besides, the bilateral kernel that is closely related to the locally adaptive regression kernel [34] is explored in recent two independent works [32,33] to replace local Gaussian smoothing of deformation field, whereby it can effectively exclude information from structures having different intensities and deformation filed pattern for discontinuity-preserved deformation reconstruction. However, the deformation reconstruction in these works did not consider the outlier problems with both missing correspondences and local large deformations. Therefore, if the outlier structures

are presented in the two images, the moving local (an)isotropic kernel function adopted in these methods [30,31,32,33] cannot be adjusted to emphasize more reliable deformation vectors from the corresponding saliency structures (called joint saliency structures, JSSs) in the two images to remove (or reduce) the outlier effects in the deformation reconstruction.

To localize the JSSs in the two images for their being emphatically grouped in mutual information (MI) based similarity measure computation, the joint saliency map (JSM) was originally proposed in our previous work [35] to reflect the global-to-local saliency structure correspondence in registration procedure, which has been proved to greatly improve the accuracy and robustness of rigid image registration with outliers. The JSM combined with keypoint clustering further obtained useful cluster-to-cluster correspondence to guide the control-point correspondence from the outlier features in the nonrigid image registration [36]. After our works, the similar mutual-saliency map [9] integrated with attribute matching was proposed to successfully remove missing correspondences in feature-based nonrigid image registration. However, matching structures with missing correspondences and local large deformations can easily introduce unrealistic distortions towards object boundaries in local subregions, which will present further complications during registration procedure by decreasing the reliability of available information. Without taking these factors into account, a structure matching approach might violate the continuity and the smoothness of structures (and their deformations) across subregions. Unfortunately, these previous JSM ideas have a clear limitation such that they cannot identify the saliency edge structures of the images to guide the continuous and smooth deformation reconstruction across object boundaries for realistic structure matching.

To solve the outlier problem with both missing correspondences and local large deformations, the proposed approach<sup>2</sup> is the first one to explicitly adopt JSS adaptive kernel regression in weighting more reliable contributions from JSS's deformation vectors at deformation reconstruction for local structure matching. This paper has the following contributions: (1) by computing the center-surround dissimilarity between neighboring local structure tensors to estimate the saliency map indicating the local saliency edge structure distribution of image, we propose new JSM based on the matching degree between the two structure-tensor-based saliency maps at every overlapping pixel pair in the two images. This JSM perfectly reflects the anisotropic JSS information, especially the joint saliency edge structures, in the two images for the ease of subsequent JSS adaptive kernel regression; (2) we propose a new JSS adaptive kernel regression for dense deformation reconstruction to explore the consistency of normal structures and their local smooth deformations surrounding the outlier structures for the problem of missing correspondences and local large deformations. Specifically, with a moving anisotropic window being oriented to be consistent with underlying JSS's structures and deformations, the output dense deformation vectors are locally estimated within an anisotropic moving window based on the specific weights of the discrete displacement vectors, which are iteratively computed from multi-resolution block matching [30,37]. In the presence of outliers, the weights of the surrounding displacement fields around the outliers are as small as possible to reduce the outlier effect on giving a distorted regression of regional dense deformations, while the JSSs and their underlying displacement fields are emphasized with their weights being kept as high as possible to ensure the accuracy of deformation reconstruction. Furthermore, the kernel function adapts its shape and orientation to reference image's local

<sup>2</sup> <http://www.escience.cn/people/bjqin/research.html>

structure in order to gather more deformation vector samples of the same structure in the kernel regression, whereby the regression of smooth deformations can be locally compliant with the underlying local saliency structures without directing the deformation across the edges and corners of local structures.

This paper is an extended version of a preliminary conference work [38]. The extensions are augmented by more detailed method descriptions, more validations and more thorough discussions for some typical cases of 2D local structure matching, which are general and common to the computer vision and pattern recognition. The rest of this paper is organized as follows. The proposed algorithm is elaborated in Section 2 followed by typical experimental results in Section 3. The whole paper is concluded in Section 4.

## 2. Methods

### 2.1. Coarse-to-fine structure matching based on block matching

The structure matching problem is formulated as an estimation of deformation of a moving image  $I_M$  with respect to a reference image  $I_R$  using transformation  $\tau$  parameterized by an unknown displacement vector  $\mathbf{t}(\mathbf{x})$ , where  $\mathbf{x}$  is the position vector in the reference image. The deformed moving image is defined by  $I_M \circ \tau(\mathbf{x}) = I_M(\mathbf{x} + \mathbf{t}(\mathbf{x}))$ . A displacement vector field describes deformation at all image pixels to maximize the similarity measure between the deformed moving image and reference image. To obtain the displacement field, our algorithm is built upon a three-step coarse-to-fine iterative block matching scheme proposed in [30]. This block matching framework is well known to deal with large deformation in nonrigid image registration. Fig. 1 displays the three-step coarse-to-fine iterative structure matching framework, where different levels have their own resolutions but the same procedure. First, the moving image  $I_M$  is deformed with an initial displacement field obtained by spatial interpolation of the output deformation field obtained on the previous level. The deformed moving image and the reference image on the current level are registered by block-matching to obtain the discrete displacement field. Second, after using the JSS adaptive kernel regression (see the green block diagrams in Fig. 1) with the kernel reflecting the edge-structure correspondence and reference structure's orientation, the structure matching scheme is to reconstruct dense current deformation field from the discrete displacement field. At last, the resulted global deformation for the iteration at next level is composed of initial deformation and current deformation by sampling the initial deformation field. The first level's initial global deformation is an affine transformation as the two images are typically already affine-registered before using our structure matching.

In the first step at each level, the moving image is deformed by an initial displacement field from previous level and sampled in the position of the sample of reference image to get deformed moving image. As in red block diagram at Fig. 1, for every pixel in deformed moving image, a block (i.e., a white neighborhood in Fig. 1) around the pixel of moving image  $I_M$  is taken and matched against a set of potential correspondent blocks in reference image. The block displacement (the red arrow in Fig. 1) that achieves the best similarity (0.65) between the blocks in moving and reference images, is stored as the discrete displacement for the original pixel. With the nature of realistic structure deformation imposing the spatial transformation to be a diffeomorphism, therefore the Jacobian of the local deformation field must be positive. This condition is preserved while only one pixel displacement is allowed for each pixel at each level of multi-resolution block matching. For every level of the multi-resolution pyramid, the final transformation is obtained by composing the transformation on the previous level with the one on the current level, in order to preserve the Jacobian positiveness condition [30].

In this study, we employ point-wise MI [39] as the local similarity measure for block matching. As a gold-standard registration criterion for two images to be registered, MI of the image intensity values of corresponding pixel pairs is maximal if the two images are geometrically aligned. The MI between the reference and moving images is defined and computed as:

$$\begin{aligned} MI &= H(R) + H(M) - H(R, M) \\ &= \sum_{i_R, i_M} p(i_R, i_M) \log \left( \frac{p(i_R, i_M)}{p(i_R)p(i_M)} \right) \end{aligned} \tag{1}$$

where  $i_R$  and  $i_M$  are image intensities of reference and moving image.  $H(I) = -\sum_i p(i) \log p(i)$  and  $H(R, M) = -\sum_{i_R, i_M} p(i_R, i_M) \log p(i_R, i_M)$  are the entropy of the intensities of image  $I$  and the entropy of the joint intensities of two images,  $p(i)$  is the intensity probabilities with  $p(i_R) = \sum_{i_M} p(i_R, i_M)$  and  $p(i_M) = \sum_{i_R} p(i_R, i_M)$ ,  $p(i_R, i_M)$  is the joint probability density function (PDF) estimated by the joint intensity histogram  $h(i_R, i_M)$ .

When the global MI of whole images can be calculated as a sum of local contribution  $S_{MI}$ , defined for each individual image pixel pair  $i_R, i_M$ , the above global MI can be rewritten as:

$$\begin{aligned} MI &= \frac{1}{N} \sum_{i_R, i_M} S_{MI}(i_R, i_M) \\ S_{MI}(i_R, i_M) &= \log \left( \frac{p(i_R, i_M)}{p(i_R)p(i_M)} \right) \end{aligned} \tag{2}$$

where the point-wise  $S_{MI}$  is calculated from the joint PDF corresponding to the whole images which have a total of  $N$  overlapping image pixels. For a given displacement, this joint PDF will be the global joint intensity histogram of the reference image with the displaced whole moving image. This is important for the multi-resolution block matching, where one pixel displacement can drastically change the PDF estimation. To estimate the optimal displacement for every pixel of moving image at multi-resolution block matching, the moving image is displaced by one pixel displacement to be overlapped with the fixed reference image, and the local evaluation of the MI can be computed just by summing the contributions of pixel pairs from the overlapped region. Therefore, at every pixel the current displacement corresponding to the biggest local MI are stored as the optimal displacement for the current deformation field estimation.

Although block matching has many advantages in obtaining the deformation of an image, implementing only this algorithm is still insufficient to avoid the irregularity of transformations such as tearing, folding and distorting in the challenging structure matching with outliers. Therefore, further reconstruction constraint is indispensable to be integrated into the registration procedure. To this end, local JSS adaptive kernel regression (as in the green block diagrams in Fig. 1) is applied into this discrete displacement fields in the second stage to reconstruct the dense deformation field: First, we compute structure tensor at each pixel position in the reference and the deformed moving images. Based on the structure tensor of reference image, the local structure adaptive anisotropic kernel is designed to spread along the direction of the local edge structure in reference image, whereby we use this anisotropic kernel's orientation information to adaptively steer the local kernel in kernel regression for dense deformation reconstruction. This scheme enables effective edge-aware deformation reconstruction that prevents the unrealistic deformation field to be smeared across object boundaries. Second, the center-surround dissimilarity between neighboring local structure tensors is explored to estimate the saliency map indicating the local saliency edge structure distribution of image. Based on the matching degree of local saliency map, the joint saliency map is constructed to emphasize the JSSs'

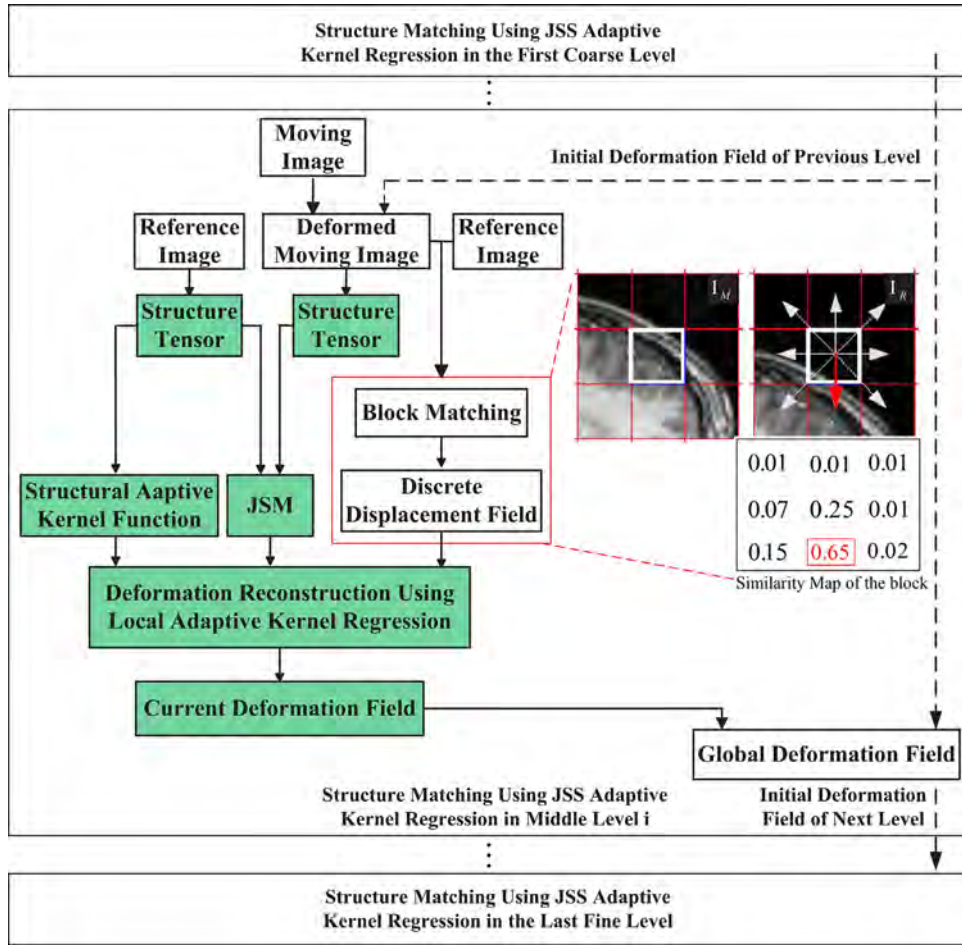


Fig. 1. Flowchart of coarse-to-fine structure matching framework. (For interpretation of the references to color in text, the reader is referred to the web version of the article.)

discrete displacement fields in the kernel regression for outlier removal. Details of the proposed approach are described in Sections 2.2–2.4. After the above-mentioned processing for each level in this coarse-to-fine framework, a smooth and dense deformation field is iteratively achieved as the global deformation at the last and finest level.

## 2.2. Kernel regression based local deformation reconstruction

Inspired by the successful applications in modern image deblurring and super-resolution imaging [30,31], we utilize kernel regression to reconstruct the smooth and dense deformation fields from the discrete displacement fields obtained through block matching. Suppose we have irregularly distributed displacement fields  $\{\mathbf{y}_i, \mathbf{x}_i\}_{i=1}^P$  given in the form

$$\mathbf{y}_i = T(\mathbf{x}_i) + \boldsymbol{\varepsilon}_i, \quad \mathbf{x}_i \in \Omega, \quad i = 1, \dots, P \quad (3)$$

where  $\mathbf{y}_i$  is a discrete displacement vector (response variable) at position (explanatory variable)  $\mathbf{x}_i$ ,  $T(\cdot)$  describes the desired dense deformation fields in the moving windows (kernel)  $\Omega$  with independent and identically distributed zero mean noise  $\boldsymbol{\varepsilon}_i = \boldsymbol{\varepsilon}(\mathbf{x}_i)$ . In statistics, the function  $T(\cdot)$  is treated as a regression of  $\mathbf{y}$  on  $\mathbf{x}$ ,  $T(\mathbf{x}) = E\{\mathbf{y}|\mathbf{x}\}$ . In this way, the reconstruction of nonrigid deformation fields is from the field of the regression techniques.

Suppose the point of interest  $\mathbf{x}$  to be reconstructed is near  $\mathbf{x}_i$ , then the regression of dense deformation field  $T(\mathbf{x}_i)$  can be approximated by a local Taylor series expansion

$$T(\mathbf{x}_i) \approx T(\mathbf{x}) + \{\nabla T(\mathbf{x})\}^T (\mathbf{x}_i - \mathbf{x}) + \frac{1}{2} (\mathbf{x}_i - \mathbf{x})^T \{\text{Hessian}[T(\mathbf{x})]\}^T \times (\mathbf{x}_i - \mathbf{x}) + \dots \approx \beta_0 + \beta_1^T (\mathbf{x}_i - \mathbf{x}) + \beta_2^T \text{vech}((\mathbf{x}_i - \mathbf{x})(\mathbf{x}_i - \mathbf{x})^T) + \dots \quad (4)$$

where  $\text{vech}(\cdot)$  is a half-vectorization operator of a symmetric matrix and  $\{\beta_0, \beta_1, \beta_2, \dots, \beta_N\}$  are  $N+1$  unknown parameters to be estimated. As in the 2D case,  $\mathbf{x} = [x_1, x_2]^T$ , we can easily estimate the unknown parameters as

$$\begin{aligned} \beta_0 &= T(\mathbf{x}) \\ \beta_1 &= \left[ \frac{\partial T(\mathbf{x})}{\partial x_1}, \frac{\partial T(\mathbf{x})}{\partial x_2} \right]^T \\ \beta_2 &= \frac{1}{2} \left[ \frac{\partial^2 T(\mathbf{x})}{\partial x_1^2}, \frac{\partial^2 T(\mathbf{x})}{\partial x_1 \partial x_2}, \frac{\partial^2 T(\mathbf{x})}{\partial x_2^2} \right]^T \\ &\dots \end{aligned} \quad (5)$$

Since we have known the discrete displacement vectors  $\{\mathbf{y}_i\}_{i=1}^P$ , we can compute  $\{\beta_n\}_{n=0}^N$  by finding the optimum solution of the following weighted least squares problem:

$$\min_{\{\beta_0, \beta_1, \beta_2, \dots\}} \sum_{i=1}^P [\mathbf{y}_i - \beta_0 - \beta_1^T (\mathbf{x}_i - \mathbf{x}) - \dots]^2 K_H(\mathbf{x}_i - \mathbf{x}) \quad (6)$$

where  $K_H(\cdot)$  is a kernel function (see the detail in the next section), which not only smoothes the approximation but also penalizes distance away from  $\mathbf{x}$ .

In addition, if we assume  $\mathbf{y}=[\mathbf{y}_1, \mathbf{y}_2, \dots, \mathbf{y}_p]^T$ ,  $\mathbf{b}=[\beta_0, \beta_1^T, \dots, \beta_N^T]^T$ , and  $\mathbf{K}=\text{diag}[K_H(\mathbf{x}_1-\mathbf{x}), K_H(\mathbf{x}_2-\mathbf{x}), \dots, K_H(\mathbf{x}_p-\mathbf{x})]$ , then we can rewrite the optimization problem in a matrix form

$$\hat{\mathbf{b}} = \underset{\mathbf{b}}{\text{argmin}} (\mathbf{y} - \mathbf{X}\mathbf{b})^T \mathbf{K}(\mathbf{y} - \mathbf{X}\mathbf{b}) \quad (7)$$

with

$$\mathbf{X} = \begin{pmatrix} 1 & (\mathbf{x}_1 - \mathbf{x}) & \text{vech}^T\{(\mathbf{x}_1 - \mathbf{x})(\mathbf{x}_1 - \mathbf{x})^T\} & \dots \\ 1 & (\mathbf{x}_2 - \mathbf{x}) & \text{vech}^T\{(\mathbf{x}_2 - \mathbf{x})(\mathbf{x}_2 - \mathbf{x})^T\} & \dots \\ \vdots & \vdots & \vdots & \vdots \\ 1 & (\mathbf{x}_p - \mathbf{x}) & \text{vech}^T\{(\mathbf{x}_p - \mathbf{x})(\mathbf{x}_p - \mathbf{x})^T\} & \dots \end{pmatrix}$$

and the least-squares estimation solution can be expressed as

$$\hat{\mathbf{b}} = (\mathbf{X}^T \mathbf{K} \mathbf{X})^{-1} \mathbf{X}^T \mathbf{K} \mathbf{y} \quad (8)$$

Because the zero-order Taylor series expansion known as the *Nadaray–Watson* estimator is sufficient to reconstruct the displacement vectors, the estimation of the deformation field at  $\mathbf{x}$  has the form

$$\hat{T}(\mathbf{x}) = \hat{\beta}_0 = \frac{\sum_{i=1}^P K_H(\mathbf{x}_i - \mathbf{x}) \mathbf{y}_i}{\sum_{i=1}^P K_H(\mathbf{x}_i - \mathbf{x})} \quad (9)$$

Since images have outliers, it is reasonable to consider uncertainty for each pixel. Therefore, we add a weight (or certainty) function  $c_i$  to Eq. (9)

$$\begin{aligned} \hat{T}(\mathbf{x}) = \hat{\beta}_0 &= \frac{\sum_{i=1}^P K_H(\mathbf{x}_i - \mathbf{x}) \cdot (\mathbf{y}_i \cdot c_i)}{\sum_{i=1}^P K_H(\mathbf{x}_i - \mathbf{x}) \cdot c_i} \\ &= \frac{\mathbf{K} \otimes (\mathbf{y} \cdot \mathbf{c})}{\mathbf{K} \otimes \mathbf{c}} \end{aligned} \quad (10)$$

The last line of Eq. (10) can also be expressed in the form of normalized convolution [30], where  $\otimes$  denotes convolution operation.

Fig. 2 illustrates the smooth displacement vectors reconstructed for every pixel in brain tumor resection region using local kernel regression. Because block matching results inherently contain incorrect matches, which are exacerbated by the outliers in the tumor resection region. As a result, the conflicts between neighboring displacement vectors (see the several red circles shown in Fig. 2(a)) widely exist in the discrete displacement fields for the tumor region. Those displacement conflicts can easily introduce the topology change of structures, such as tearing and distorting. Fortunately, all the displacement vector conflicts are removed or smoothed by the local kernel regression in Fig. 2(b), where the displacement vectors having opposite directions fully disappear with the displacement magnitudes simultaneously being smoothed. Next, to match local structures in the presence of outliers, we design structural adaptive kernel function and robust weighing scheme for the moving window to further boost the accuracy and robustness of the local deformation reconstruction.

### 2.3. Local structure-adaptive kernel function

As a crucial component of local kernel regression, the shape of the kernel function (or moving window) determines the spatial distribution of samples which are gathered for the quality of the locally reconstructed signal. In principle, isotropic Gaussian kernels are mostly used as kernel functions in nonparametric regression. However, traditional isotropic Gaussian kernels are insufficient to cover more samples of the same modality along some specific orientations in signal reconstruction. Besides, Gaussian kernels' fixed

scales and orientations can neither detect nor enhance edge structures. These factors easily cause diffusion across object boundaries. To remedy these restrictions, Pham et al. proposed an anisotropic kernel function to adapt its shape to the density of sampling [40]. Afterwards, Takeda et al. [41] utilized gradient covariance matrices to construct steering kernels, which have been proved to possess the ability to capture the edges of an image and be extremely robust to noise and perturbations of the data.

In dense deformation reconstruction, the desirable local kernel function is assumed to be extended along local structure orientation in the reference image so that it can gather more samples of discrete displacement vectors that correspond to the same saliency structure in the reference image. Besides, the kernel function contracts in the normal orientation of local saliency structure to prevent deformation diffusion across the edges between the different structures. Based on these schemes, it can effectively reduce the risk of changing the topology of the local saliency structures in the kernel regression. Considering that local structure tensor (LST) represents the anisotropic local saliency structure information of an image [42], we therefore design local structure-adaptive kernel functions using the LST information in the reference image.

Before designing a local structure-adaptive kernel function at a certain pixel, we must compute LST in advance to grasp the local saliency structure around that pixel in 2D image. We assume that  $I(\mathbf{x})$  denotes the intensity value at point  $\mathbf{x}(x, y)$ , the gradient information is expressed as  $I_x = \partial I / \partial x$ ,  $I_y = \partial I / \partial y$ , and  $\nabla I(\mathbf{x}) = [I_x \ I_y]^T$  indicates the local gradient vector, then the gradient structure tensor (GST) in 2D case can be described as

$$\text{GST}(\mathbf{x}) = \nabla I(\mathbf{x}) \nabla I(\mathbf{x})^T = \begin{pmatrix} I_x^2 & I_x I_y \\ I_x I_y & I_y^2 \end{pmatrix} \quad (11)$$

Generally, to integrate the surrounding structural information from neighborhoods, the GST is smoothed by a Gaussian filter to derive the LST. The scale  $\sigma$  of the Gaussian filter is half the filter window size, namely  $\sigma = 1.5$ , because the size of the filter window in our experiments is  $3 \times 3$  pixels. Therefore, we derive the LST from GST and perform a principal component analysis of the LST as follows:

$$\text{LST}(\mathbf{x}) = G_\sigma * \text{GST}(\mathbf{x}) = \begin{pmatrix} G_\sigma * I_x^2 & G_\sigma * I_x I_y \\ G_\sigma * I_x I_y & G_\sigma * I_y^2 \end{pmatrix} = \lambda_u \mathbf{u} \mathbf{u}^T + \lambda_v \mathbf{v} \mathbf{v}^T \quad (12)$$

where  $\{\lambda_u, \lambda_v\}$  ( $\lambda_u \geq \lambda_v$ ) are the eigenvalues with the corresponding eigenvectors being  $\{\mathbf{u}, \mathbf{v}\}$ . These eigenvectors contain the information about the local orientation distribution, in which pixel values change fastest along  $\mathbf{u}$  direction while they change slowest along  $\mathbf{v}$ . Moreover, eigenvalues reflect both intensity variation in each direction and morphological information of a local region. For example in 2D image,  $\lambda_u \approx \lambda_v \approx 0$  corresponds to a homogenous region with no measurable structure,  $\lambda_u \gg \lambda_v \approx 0$  describes linear structure while  $\lambda_u \geq \lambda_v \gg 0$  appears at corner structure.

With the above-mentioned LST computation in mind, we design the kernel function to meet the following requirements: for regions containing obvious structural information such as histologic margins in a medical image, the kernels should be anisotropic with the regression computation being enhanced just along the main orientation and being suppressed along other orientations; for homogeneous regions without distinct structural information, the kernel should be isotropic with the regression computation being equal in all direction. We assume that  $\mathbf{x}_0$  denotes a central position in 2D image,  $\mathbf{x}$  is a position in its neighborhood,  $\{\mathbf{u}, \mathbf{v}\}$  are the eigenvectors of  $\text{LST}(\mathbf{x}_0)$  and  $\{\lambda_u, \lambda_v\}$  are the corresponding eigenvalues

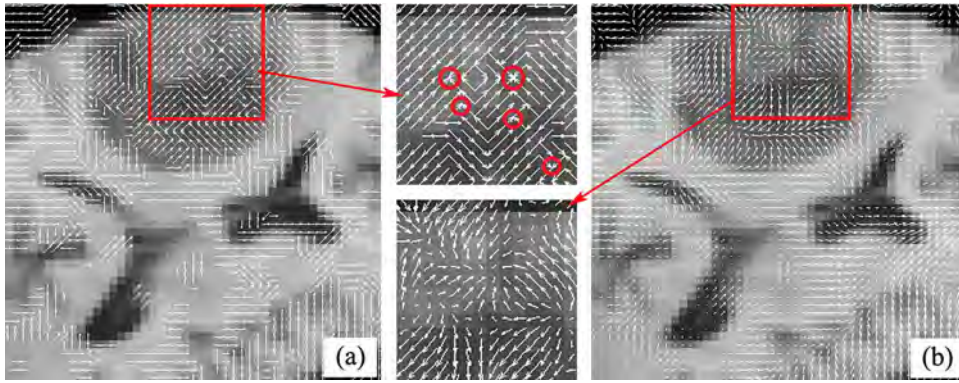


**Fig. 2.** Application of kernel regression in deformation reconstruction. (a) The conflicts between neighboring displacement vectors (several red circles) widely exist in the discrete displacement field for the tumor region. (b) The displacement vector conflicts are removed or smoothed by the local kernel regression along with the displacement magnitudes simultaneously being smoothed. (For interpretation of the references to color in this legend, the reader is referred to the web version of the article.)

of  $\{u, v\}$ , thus a local structure-adaptive Gaussian kernel in 2D case is designed as

$$a(x, \mathbf{x}_0) = \frac{1}{2\pi\sigma_u\sigma_v} \exp \left[ - \left( \frac{\mathbf{d}_u^2}{2\sigma_u} + \frac{\mathbf{d}_v^2}{2\sigma_v} \right) \right] \quad (13)$$

$$\mathbf{d}_u = \langle \mathbf{d}, \mathbf{u} \rangle, \quad \mathbf{d}_v = \langle \mathbf{d}, \mathbf{v} \rangle, \quad \mathbf{d} = \mathbf{x} - \mathbf{x}_0$$

where  $\mathbf{d}$  is the vector from  $\mathbf{x}_0$  to  $\mathbf{x}$ ,  $\langle \mathbf{d}_u, \mathbf{d}_v \rangle$  are the projections of the vector  $\mathbf{d}$  on  $\{u, v\}$ , and the directional scales of the Gaussian kernel  $\{\sigma_u, \sigma_v\}$  are determined by the anisotropy  $A$  as follows:

$$\sigma_u = \frac{\alpha}{\alpha + A} \sigma_c, \quad \sigma_v = \frac{\alpha + A}{\alpha} \sigma_c \quad (14)$$

where  $A = (\lambda_u - \lambda_v) / (\lambda_u + \lambda_v)$ . The two directional scales of the Gaussian kernel can be adjusted by the parameter  $\alpha > 0$  and the local scale  $\sigma_c$ . Specifically,  $\alpha$  determines the eccentricity of the kernel while  $\sigma_c$  affects the number of discrete vectors that contribute to the reconstruction of continuous deformation vectors. For the sake of simplicity, the local scale is set to half the neighborhood window size for each kernel according to our experience. Therefore, we set  $\alpha = 0.5$  and  $\sigma_c = 1.5$  because we utilize a  $3 \times 3$  pixel neighborhood window in our experiments.

Two kernel functions for two distinct image structures are displayed at the doll images in Fig. 3, where the crosses indicate two different kinds of typical image structures (blue cross for border and red cross for homogeneous region). In Fig. 3, the two pairs of orthogonal vectors indicate the main axes of their corresponding Gaussian kernels (blue cross at Fig. 3(c) and red cross at Fig. 3(d)). The length of the vector is determined by the scale in the direction of the vector.

Fig. 4 illustratively explains why we prefer local structure-adaptive kernel to isotropic kernel in our structure-adaptive kernel regression. The regions pointed by red arrows are small scale structures which have local large deformations. The directions of the displacement vectors (spaced every 5 pixels) in these small structures are inevitably conflicted with those of the large deformations of the neighboring structures. These deformation conflicts that are introduced by the opposite displacement vectors can easily cause tearing, folding or distorting of the local small scale structures. For example, the eyes in Fig. 4(c) display distortion owing to the conflict of the deformation directions displayed in Fig. 4(e). Comparatively, our local structure-adaptive kernels suppress the contributions of the displacement vectors which are not consistent with the structure orientation, the deformation conflicts are therefore removed in Fig. 4(f) with no distortion existing in the eyes at Fig. 4(d).

Fig. 4(h) demonstrates the overview of mesh deformation (10 pixels vertex spacing) in the local structure-adaptive kernel regression, which can produce the smooth adaptivity of local mesh

deformation to the local anisotropic structures. Obviously, this local structure-adaptive kernel regression obtains smooth mesh boundaries which are consistent with the local structures' boundaries. However, isotropic kernels in kernel regression easily produce irregularly deformed local meshes which are not adaptive to the local structures, so that it is very difficult to identify boundaries of local structures from the non-smooth mesh deformation in Fig. 4(g).

#### 2.4. Robust weighting mechanism using JSM

In kernel regression, the weight function  $c(\mathbf{x})$ , between 0 and 1, specifies the reliability (or certainty) at  $\mathbf{x}$  for the local estimation in a moving window and always describes the spatial dependence in the locally varying special context. With locally data-dependent weights, recently popularized and very effective image filters are developed in image and video processing field [28,29]. Since the region with saliency structure information has real influence over locally adaptive image processing based on kernel regression, Suarez et al. [30] proposed a weighting scheme in the kernel regression of registration transformations by using the scalar measure of a local structure in reference image. However, for nonrigid image registration, the salient structural regions in reference image may introduce non-corresponding salient structural regions at same locations in moving image. Therefore, the method proposed by Suarez et al. is most likely to assign wrong high weights to the saliency structures that have missing correspondences.

To avoid the above-mentioned mis-assignment and minimize the outlier effect on the deformation reconstruction, we propose a robust weighting mechanism by simultaneously considering the matching degree of local saliency structures in the overlapping parts of the two images. We deploy the concept of JSM into our robust weighting mechanism and pay more attention to the JSSs in the two images. The JSSs and their incurring deformations should be emphatically treated in the local kernel regression to reconstruct the dense deformation fields from the discrete displacement fields that contain outliers.

With the general JSM-based weighting scheme in mind, we first construct a saliency map to indicate the local saliency structure distribution in each image. Since the LSTs mentioned in Section 2.3 contain sufficient structural information in a region, we can reasonably use them to reflect the saliency map of an image. Inspired by the center-surround mechanism [43] which has defined the intensity-contrast-based visual saliency map, we define a saliency operator based on the contrast among neighboring ( $3 \times 3$  pixels) structure tensors. This contrast emphasizes the dissimilarity or discrepancy between neighboring local structure tensors. Specifically,

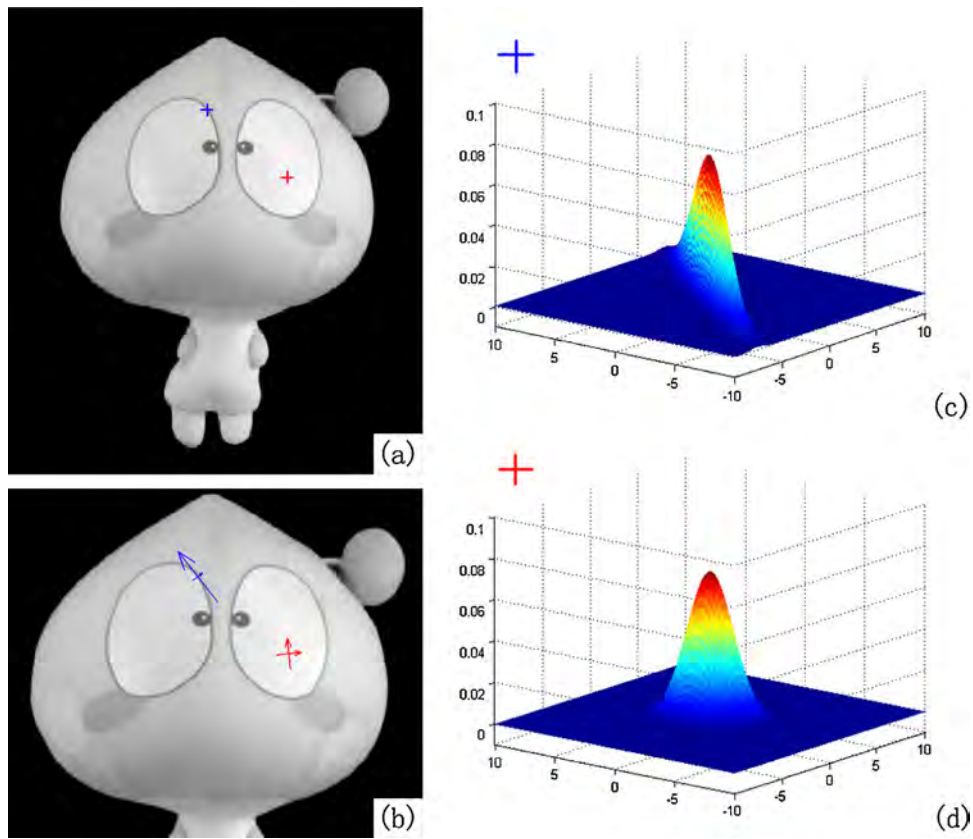


**Fig. 3.** Gaussian kernels designed for different image local structures. (a) Two labeled positions (red cross and blue one). (b) The scales and orientations of Gaussian Kernels in corresponding positions. (c) Gaussian kernel for the region with blue cross. (d) Gaussian kernel for the region with red cross. (For interpretation of the references to color in this legend, the reader is referred to the web version of the article.)

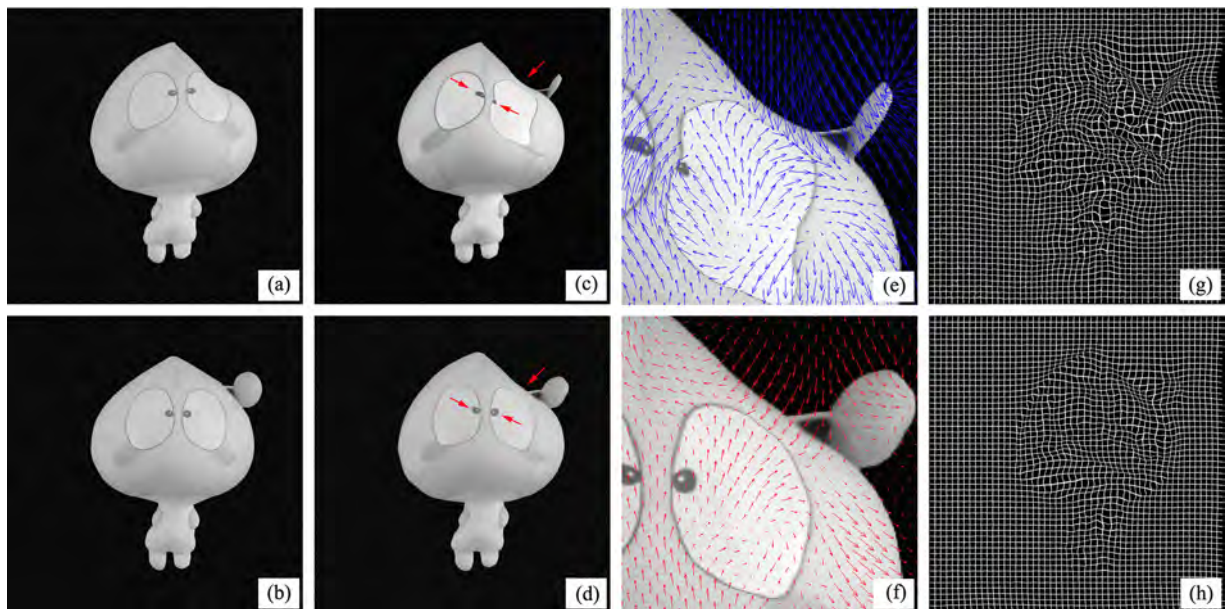


**Fig. 4.** Comparison between using isotropic kernels and using local structure-adaptive kernels in kernel regression based deformation reconstruction. (a) and (b) The reference and moving images. (c) and (d) Isotropic kernels in kernel regression introduce eye distortions (red arrow) in registered moving image, while local structure-adaptive kernels can remove these distortions. (e) and (f) Isotropic kernels produce the deformation conflicts in the displacement vector fields, while local structure-adaptive kernels remove these conflicts. (g) and (h) Isotropic kernels easily produce irregularly deformed local meshes, while local structure-adaptive kernels achieve the smooth adaptivity of local mesh deformation to the local anisotropic structures. (For interpretation of the references to color in this legend, the reader is referred to the web version of the article.)

for a given point  $\mathbf{x}_0$  and its neighborhood  $\Omega$ , the saliency value  $S(\mathbf{x}_0)$  at  $\mathbf{x}_0$  in a saliency map can be computed through

$$S(\mathbf{x}_0) = \text{avg} \sum_{\mathbf{x} \in \Omega} \|\text{LST}(\mathbf{x}) - \text{LST}(\mathbf{x}_0)\|_D \quad (15)$$

where  $\|\cdot\|_D$  defines a distance metric describing the dissimilarity between two LSTs, which is detailed in the following section. The operator **avg** computes the average of the dissimilarities within the neighborhood  $\Omega$  of  $\mathbf{x}_0$ . Traditional tensor similarity measures such as fractional anisotropy (FA) and cosine similarity measure are not appropriate for defining tensor-based saliency operator because they only compare either scales or orientations of two tensors. Fortunately, a few improved tensor similarity measures computing both scales and orientations of two tensors have been reported. In [44], Zhang et al. introduced diffusion tensor metric, which is defined as

$$\|\mathbf{T}_1 - \mathbf{T}_2\|_D = \sqrt{\frac{8\pi}{15} (\|\mathbf{T}_1 - \mathbf{T}_2\|_C^2 - \frac{1}{3} \text{Tr}^2(\mathbf{T}_1 - \mathbf{T}_2))} \quad (16)$$

where  $\|\mathbf{T}_1 - \mathbf{T}_2\|_C = \sqrt{\text{Tr}(\mathbf{T}_1 - \mathbf{T}_2)^2}$  is the Euclidean distance between two tensors  $\{\mathbf{T}_1, \mathbf{T}_2\}$ , **Tr** is the operator for computing the trace of matrix.

In a tensor-based saliency map, the saliency value is a general representation of the local edge structure distribution in an image. Low saliency values always appear in the homogeneous and background regions while high saliency values are assigned to the edge structures owing to the highlighted contrast among neighboring

LSTs in these regions. After the two normalized saliency maps were achieved to indicate the local edge structure distribution, JSM is ready to describe the matching degree between the two saliency maps at every pixel pair in the overlapping regions of the two images. Given a point  $\mathbf{x}_R$  in the reference image and its corresponding point  $\mathbf{x}_M$  in the moving image after initial transformation, their joint-saliency value in a JSM is defined as

$$JS(\mathbf{x}_R, \mathbf{x}_M) = \min\{S_R(\mathbf{x}_R), S_M(\mathbf{x}_M)\} \frac{A \cdot B}{B + \|\text{LST}(\mathbf{x}_R) - \text{LST}(\mathbf{x}_M)\|_D} \quad (17)$$

where  $\{S_R(\cdot), S_M(\cdot)\}$  denote the saliency values in the saliency maps of the reference and the moving images, respectively. The empirical parameters  $A$  and  $B$  are used to normalize the JSM values into a final value between 0 and 1 for the definition of weight function  $c(\mathbf{x})$ . In our experiments,  $A = 10$  and  $B = \frac{1}{2} \max(\|\text{LST}(\mathbf{x}_R) - \text{LST}(\mathbf{x}_M)\|_D)$ , in which  $B$  is half the maximum dissimilarity value between two LSTs in the whole overlapped regions of the two images. It should be noted that it may introduce a situation that both of the corresponding pixels are set to high saliency values in the saliency maps, while their local variations of gradient orientations are in fact totally different. To avoid this situation, we also consider the dissimilarity measure between  $\text{LST}(\mathbf{x}_R)$  and  $\text{LST}(\mathbf{x}_M)$  at the denominator in Eq. (17).

Fig. 5 shows some examples of normalized JSM with the color scale representing different joint saliency values. The high joint saliency values represented by red color suggest that the underlying pixel pairs come from the JSSs. On the contrary, the regions with low JSM values are rendered in blue color, which indicates that the

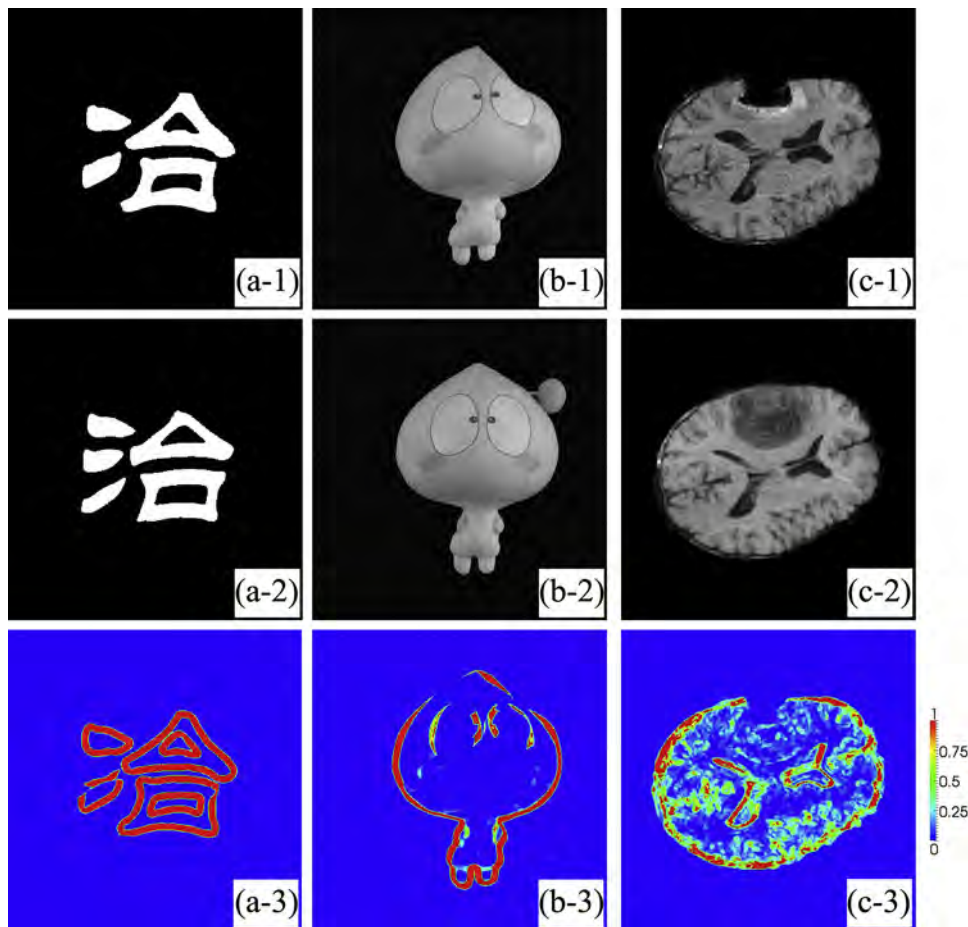


**Fig. 5.** JSM Examples with color scale representing different joint saliency values. Each column shows one case. The reference images and the moving ones are shown at the top and middle rows. Their JSMs are displayed at the bottom row where the red regions correspond to the higher joint saliency values while the blue regions correspond to the lower joint saliency values. (For interpretation of the references to color in this legend, the reader is referred to the web version of the article.)

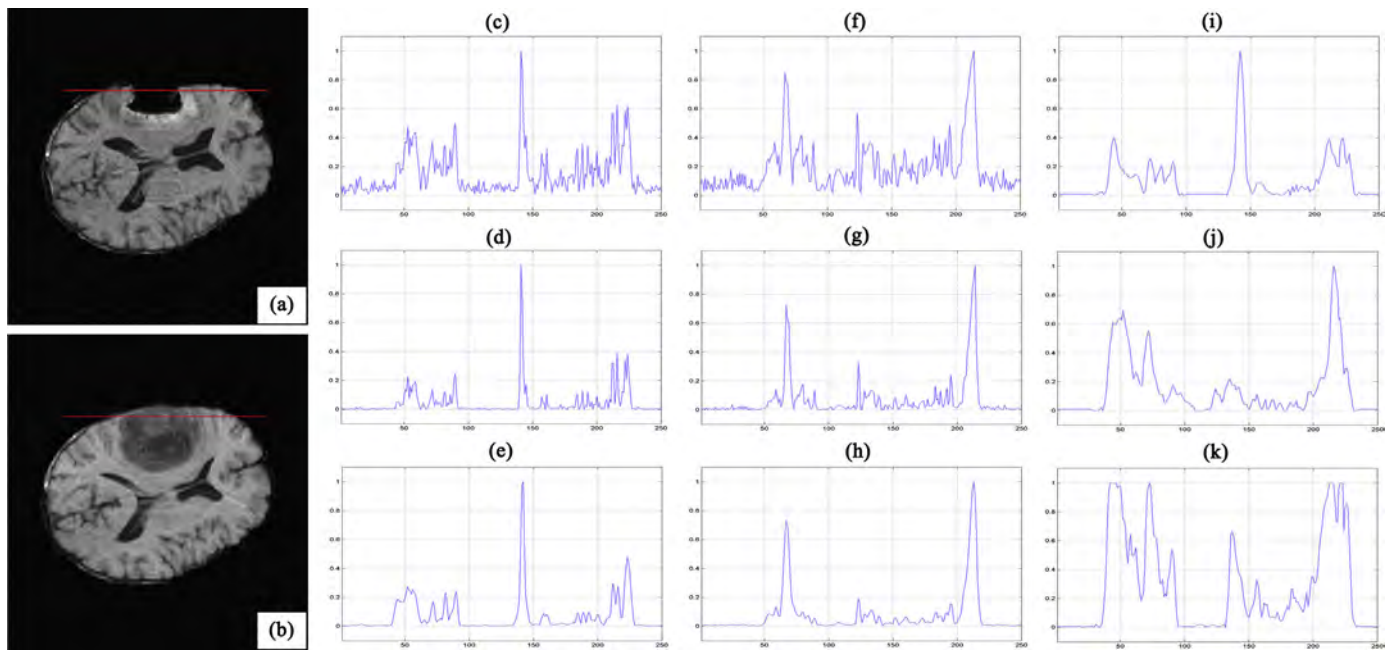


**Fig. 6.** The reference and the moving images and their gradient magnitude, largest eigenvalue profiles for GST and LST, and the JSM magnitude. (a) and (b) The reference and moving images. (c)–(e) Gradient magnitude profiles, largest eigenvalue profiles of GST and largest eigenvalue profiles of LST of the red line in (a). (f) and (h) Gradient magnitude profiles, largest eigenvalue profiles of GST and largest eigenvalue profiles of LST of the red line in (b). (i) and (j) Saliency value profiles of the red lines in (a) and (b). (k) JSM value profiles of the red lines in (a) and (b). (For interpretation of the references to color in this legend, the reader is referred to the web version of the article.)

underlying pixel pairs originate from either homogeneous regions or outlier regions. The discrete displacement vectors in these red JSS regions are expected to contribute more to the kernel regression than the blue regions having low JSM values, this weighting scheme is therefore called JSS adaptive kernel regression for nonrigid image registration.

The JSM in our study mainly responds to the corresponding high-gradient edge pixels. However, it does not simply highlight the common image gradients in the two images. Fig. 6 vividly presents the differences between the image gradient magnitude, the largest eigenvalue of GSTs and LSTs, the saliency value and the JSM value profiles of the same red line at the two images (Fig. 6(a) and (b)). For easy comparison, the range of ordinates in Fig. 6(c)–(k) are bound to [0, 1]. As shown in Fig. 6, the image gradient features in Fig. 6(c) and Fig. 6(f) for the two images are very sensitive to noise and do not agree with each other at each overlapping location. The noise sensitivity is gradually reduced by using the GSTs (Fig. 6(d) and (g)) and the LSTs (Fig. 6(e) and (h)). The saliency values of the two images in Fig. 6(i) and (j) are robust to noise due to their computing the regional contrast of LSTs through Eq. (15). Moreover, the structural image information in a large region is also comprehensively considered according to Eq. (15). As a result, the JSM values (Fig. 6(k)) computed through the saliency values can accurately preserve the JSSs in larger capture range with smaller variability than the image gradients. Therefore, the effectiveness of JSM is strongly confirmed in Fig. 6.

Because of the outliers introduced by missing correspondences, local large deformations and incorrect block matching, the dense deformation fields cannot be simply interpolated from the discrete displacement vectors in block matching. The JSS adaptive kernel regression is used to reconstruct the dense deformation fields from the discrete displacement vectors, i.e., smooth the outlier effects on the deformation reconstruction. Due to the expected deformations in the outlier region being consistent with its neighboring deformations, the JSM values in the neighboring regions are used to assign different weights to the different displacements of the neighboring structures, only those neighboring deformations with

high JSM values indicating the consistency in structure orientations are given high weights in kernel regression based deformation reconstruction.

Fig. 7 illustrates an improvement on the deformation field reconstruction after introducing the JSM-based local JSS adaptive kernel regression. The region pointed by red arrows in Fig. 7(c) and (d) is outlier region with missing correspondences and local large deformations. Without JSM-based robust weighting mechanism, the converged displacement vectors (5 pixels spacing) from conflicting directions (see Fig. 7(e)) in the outlier region spread the distortion effect into the eye region (see Fig. 7(c)). Due to the JSM-based robust weighting mechanism introducing weighted smoothing effect on the magnitudes and directions of displacement vectors (see Fig. 7(f)), moving image's eye distortion is removed (see Fig. 7(d)) with the outlier structure deformations being simultaneously matched to those of the reference image (see Fig. 7(f)). Compared with the deformation meshes (10 pixels vertex spacing) in Fig. 7(g), the deformation meshes at Fig. 7(h) display the overall smoothness improvement for the structural deformations at the outlier structures due to the JSM-based robust weighting mechanism.

### 3. Experimental results

To validate the proposed algorithm<sup>3</sup> on some challenging images with missing correspondences and local large deformations, we make a comparison among the proposed algorithm and other state-of-the-art intensity-based nonrigid registration methods using some typical 2D image sets, where the moving images with a variety of outlier structures should be matched into the reference images.

We choose ANTs<sup>4</sup> with geodesic symmetric normalization (Syn) diffeomorphic transformation and MI (AGS1) [45], ANTs

<sup>3</sup> <http://www.esience.cn/people/bjqin/research.html>

<sup>4</sup> <http://www.picsl.upenn.edu/ANTs>

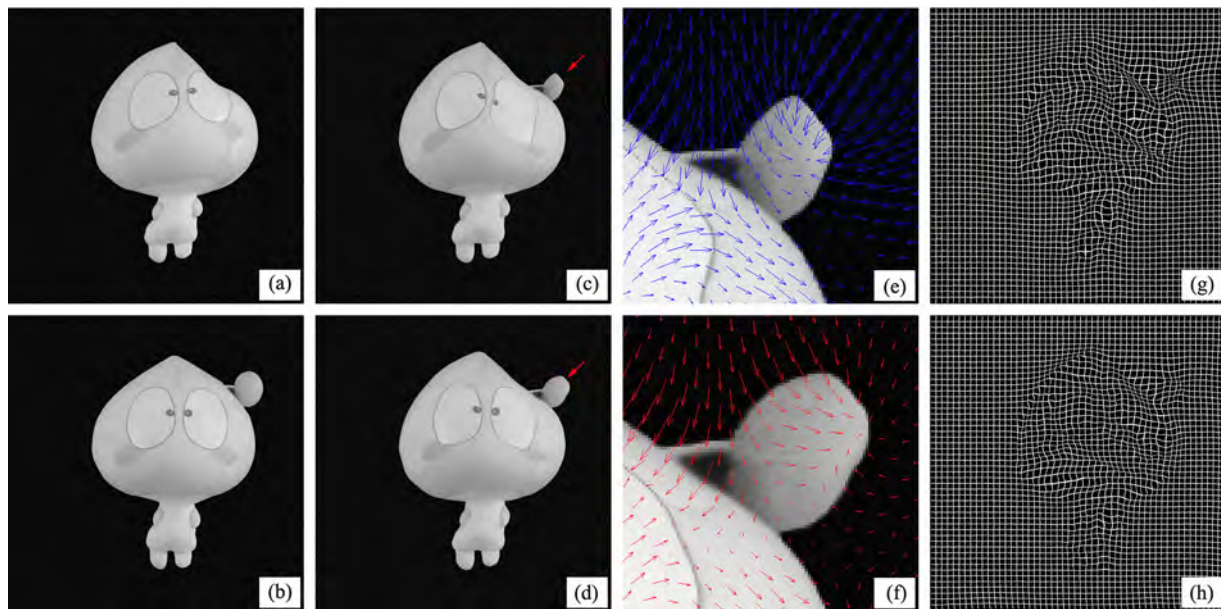


**Fig. 7.** Matching performance improvement through JSM-based robust weighting mechanism. (a) and (b) The reference and moving image. (c) and (d) The conflicting deformations in the outlier region (red arrows) spread the distortion effect into the eyes, this moving image's eye distortion is removed in (d) by JSM-based weighting mechanism. (e) and (f) There are converged displacement vectors from conflicting directions in (e), these conflicting displacement vectors in outlier region in (f) are simultaneously matched to those of the reference image through JSM-based weighting mechanism. (g) and (h) There is smoothness improvement in the deformation mesh from (g) to (h) if using JSM-based robust weighting mechanism. (For interpretation of the references to color in this legend, the reader is referred to the web version of the article.)

with greedy Syn diffeomorphic transformation and MI (AGS2), and ANTs with elastic transformation and MI (AMI) in gradient descent and multi-resolution optimization framework. We also include diffeomorphic Demons with diffusion-like regularization (DDD)<sup>5</sup> [46], fast B-spline with MI (BMI),<sup>6</sup> AMI with cost-function masking (AMM), edge-preserving PatchMatch optical flow (EPPM) algorithm<sup>7</sup> [47], large displacement optical flow (LDOF) algorithm<sup>8</sup> [2] and flexible variational non-linear intensity-based (FVNI) method<sup>9</sup> [48]. Our method uses the following parameters: the number of pyramid levels is 5; the local similarity measure is MI. AGS1 and AGS2 have the following parameters: the histogram bin size is 32; the number of pyramid levels is 3; the iterations are set to  $100 \times 100 \times 10$ ; the gradient step is 0.1. Besides, AGS1 sets the time points to 3 for full time velocity field optimization with integration step being 0, AGS2 sets the default regularization to Gaussian filtering with a sigma of 3. We set the parameters of AMI and AMM as follows: the histogram bin size is 32; the number of pyramid levels is 3; the iterations are set to  $100 \times 100 \times 10$ ; the gradient step is 10; the default regularization is Gaussian filtering with a sigma of 3. The parameters of DDD method are set as follows: the variance of smoothing kernels is 2; the step scale is 1; the number of pyramid levels is 5; the number of iterations is 100. The parameters of the BMI method are selected as follows: the number of iterations is set to 100; the grid size is 15; the histogram bin size is 32; the spatial sample is 50,000; the maximum deformation is 20. The EPPM uses the default parameters: patch radius  $r=17$ ; the spatial and range influence parameters are  $\sigma_s=0.2r$  and  $\sigma_r=0.1$ , respectively. We choose the following default parameters of the LDOF method: the tuning parameters for regularity constraint, the point correspondence constraint and the

constraint on the gradient are 30, 300 and 5; downsampling factor is 0.95; the numbers of outer iterations and inner iterations are set to 10 and 5. The parameters of FVNI are as follows: the force term is Demons forces with diffusion regularization; the regularizer parameter alpha is 0.5; the number of multi-resolution levels is 3; the maximum number of each iteration is 400; time step is 1.0; the stop criterion slope is 0.005. With those parameters all the methods mentioned above achieve their best performances.

To evaluate the performance of the 10 competing methods, both registration accuracy and efficiency are estimated during the assessment. The registration accuracy of binary image pairs is validated based on the discrepancies from the difference image between the reference and the registered moving images. However, the evaluation based on the difference image is not reliable for grayscale image registration [49]. Due to the registration errors measured at densely distributed landmarks being considered as the standard for evaluating registration accuracy of grayscale images, we manually selected a large number of appropriate landmark pairs in the reference and the registered moving images (especially in the normal structural regions close to the outliers). The selected landmark pairs fully exclude outlier features but identify some corresponding small scale saliency structures (having local large deformations) around the outlier regions. Therefore, the matching accuracies of 10 registration methods can be assessed with the mean registration error (MRE) and standard deviation (SD) [49] between these selected landmark pairs. However, due to the missing correspondences in the outlier structures, we are unable to define sufficient corresponding landmark pairs within and around the outlier structures and therefore cannot fully evaluate the matching performance in these outlier structures. This limitation of landmark-based evaluation is demonstrated in the following section when we evaluate the matching performance for challenging outlier structures.

The reference and the moving binary images in the first experiment are two similar Chinese characters at Fig. 8(a) and (b). The two strokes in the left part of the reference image correspond to the upper left and lower left ones in the moving image, while the

<sup>5</sup> <http://mipav.cit.nih.gov>

<sup>6</sup> <http://www.slicer.org>

<sup>7</sup> <https://sites.google.com/site/linchaobao/home/eppm>

<sup>8</sup> <http://www.cs.berkeley.edu/katef/LDOF.html>

<sup>9</sup> <http://hdl.handle.net/10380/3460>

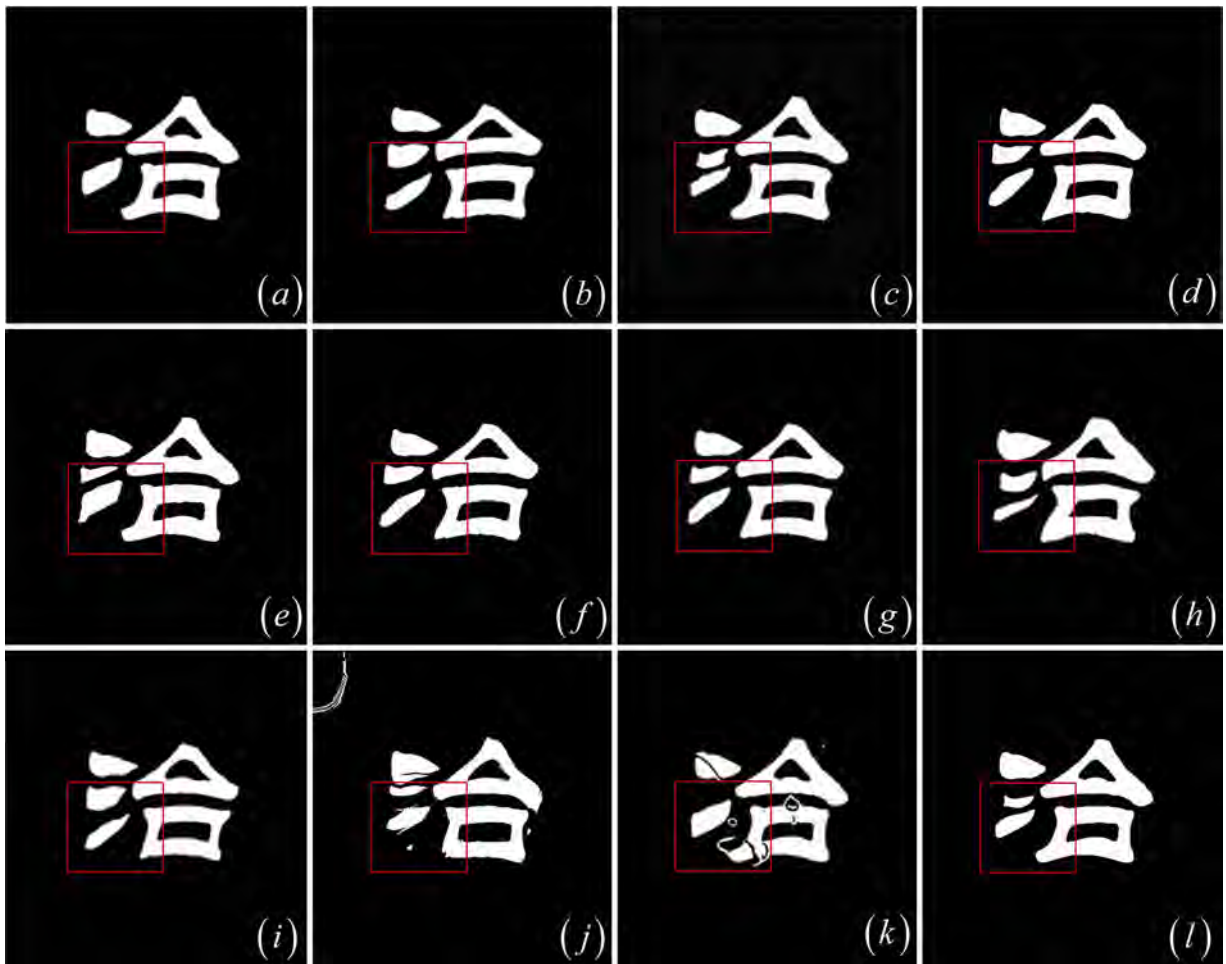


**Fig. 8.** Chinese character image registration. Our method, AGS2 and the FVNI methods have clearly outperformed the other methods. (a) and (b) The reference and moving images, (c) ours, (d) AGS1, (e) AGS2, (f) AMI, (g) DDD, (h) BMI, (i) AMM, (j) EPPM, (k) LDOF, (l) FVNI. (For interpretation of the references to color in text, the reader is referred to the web version of the article.)

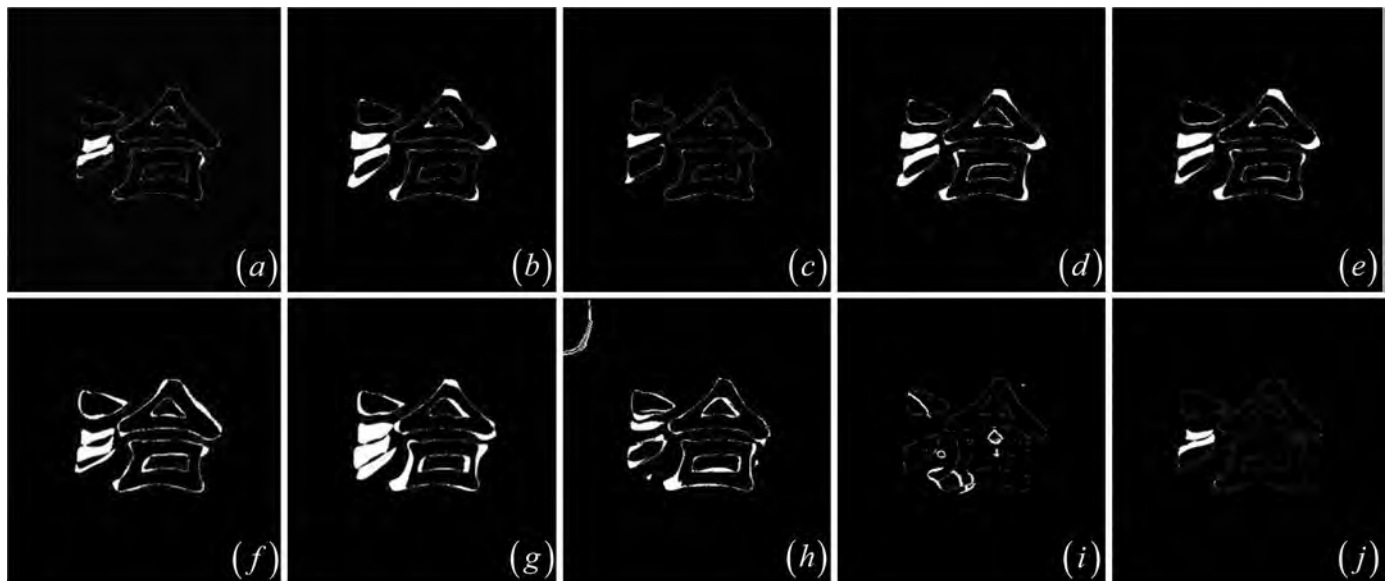


**Fig. 9.** Difference images of Chinese characters from the 10 matching results. (a) Ours, (b) AGS1, (c) AGS2, (d) AMI, (e) DDD, (f) BMI, (g) AMM, (h) EPPM, (i) LDOF, (j) FVNI.

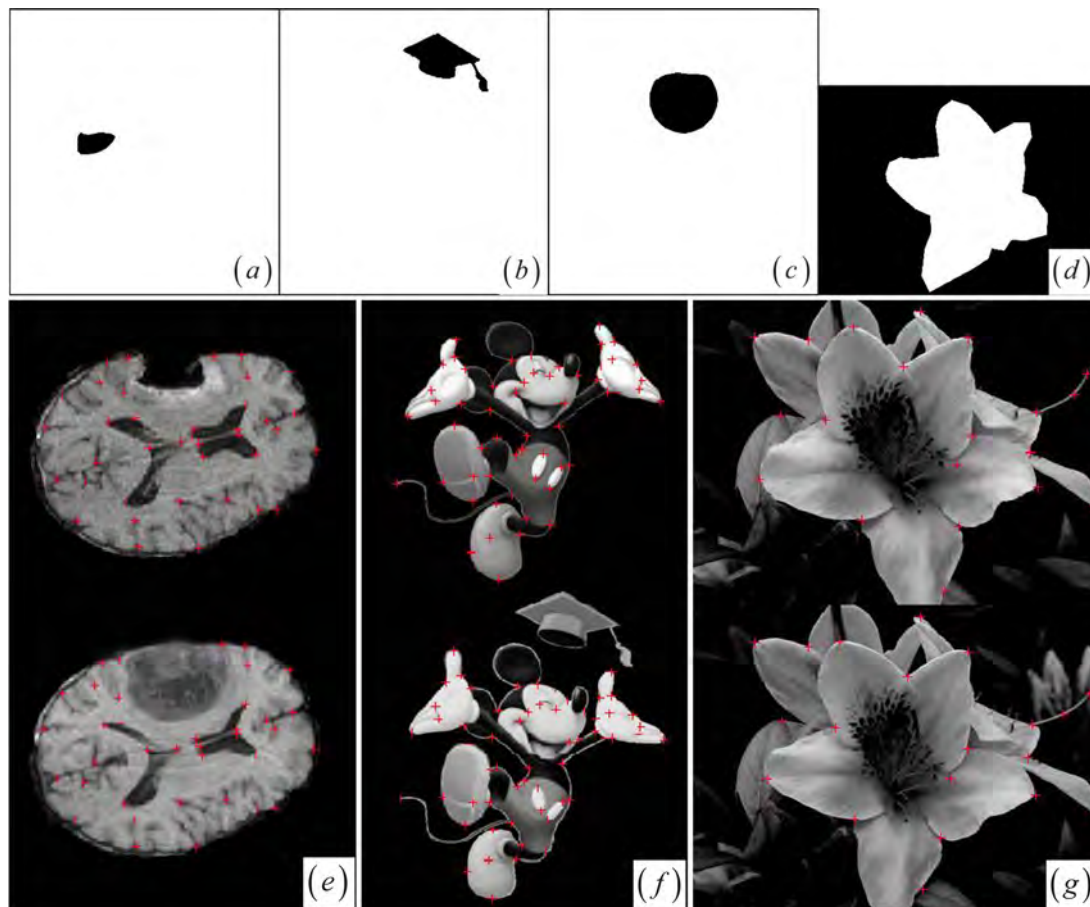


**Fig. 10.** Masks and Landmark pairs for the images. (a) and (d) The black mask definitions for Chinese characters, Mickey, brain tumor and flower images. (e)–(g) The corresponding landmark pairs for Mickey, brain tumor and flower images in landmark-based registration error evaluation. (For interpretation of the references to color in text, the reader is referred to the web version of the article.)

middle stroke (outlier) in the left part of moving image has missing correspondence (see the red boxes in Fig. 8(a) and (b)). Moreover, the triangular and the rectangular openings at the right part of the character are narrowed. The local large deformations are apparent at lower left corner of the rectangular region and low right corner of the triangular region. Besides, the lower left stroke from southwest to northeast is lengthened with counter-clockwise rotation. Fig. 8(c)–(l) are the registered results of the 10 methods. The strokes at the left part and the corner regions of the two openings are locally deformed more or less in the 10 matched images. However, only our method, AGS2 and FVNI (Fig. 8(c), (e) and (l)) methods have clearly outperformed the other methods. The performance advantages of our approach, AGS2 and FVNI (Fig. 9(a), (c) and (j)) methods over other methods can be clearly validated from the difference images in Fig. 9, where the smaller white regions in difference image mean the better structure matching performances. The matching results from the two large displacement optical flow methods EPPM and LDOF have changed the topology of moving image by removing the middle stroke in the left part and introducing some obvious artifacts in the characters at Fig. 8(j) and (k).

Though the constrained cost-function masking has masked the middle stroke in moving image (see the mask definition in Fig. 10(a)), without robust scheme tackling missing correspondences and local large deformations simultaneously, the AMM method (Figs. 8(i) and 9(g)) even performs a little worse than the AMI method (Figs. 8(f) and 9(d)), especially in matching the local structural regions with local large deformations in Fig. 9(g). It is clear from these 10 results that the proposed, AGS2 and FVNI methods have produced the satisfactory structure matching.

The second experiment involves aligning two grayscale Mickey images (Fig. 11(a) and (b)) with an outlier doctoral in the moving image. Moreover, there are large deformations in Mickey's left thumb, left hand, right thumb (see the red boxes in Fig. 11), right shoe and right button in Mickey's belly. Consequently, the visual and the subsequent landmark-based validations of the performances of these registration methods are largely dependent on the deformed results of these structures. Fig. 11(c)–(l) show that the proposed (Fig. 11(c)) and FVNI (Fig. 11(l)) methods outperform the other methods by perfectly deforming the local structures to desired positions, though the FVNI method has introduced rounding image artifact (see the bottom red box in Fig. 11(l)) around the right button in Mickey's belly. In contrast, the morphology of Mickey's left hand is changed by AGS1 (Fig. 11(d)), AGS2 (Fig. 11(e)), AMI (Fig. 11(f)) and AMM (Fig. 11(i)) methods. Mickey's left thumb, right shoe and right button in Fig. 11(g) have not deformed by DDD method. Mickey's left thumb has not deformed and the left palm become thicker in Fig. 11(h) after BMI registration. In this experiment, though with the constrained cost-function masking for the doctoral hat (see the mask definition in Fig. 10(b)), AMM method has no improvement in matching local structures (Fig. 11(i)). The EPPM method (Fig. 11(j)) produces poor matching results in the hands, hat, belly and tail of the Mickey compared to the LDOF method (Fig. 11(k)) which introduces undesired artifacts in right thumb and hat of the Mickey.

Another grayscale image registration is matching post-operative (Fig. 12(a)) and pre-operative (Fig. 12(b)) brain tumor images. Brain tissue severely suppressed by tumor in the pre-operative image expands after tumor resection, which not only brings missing

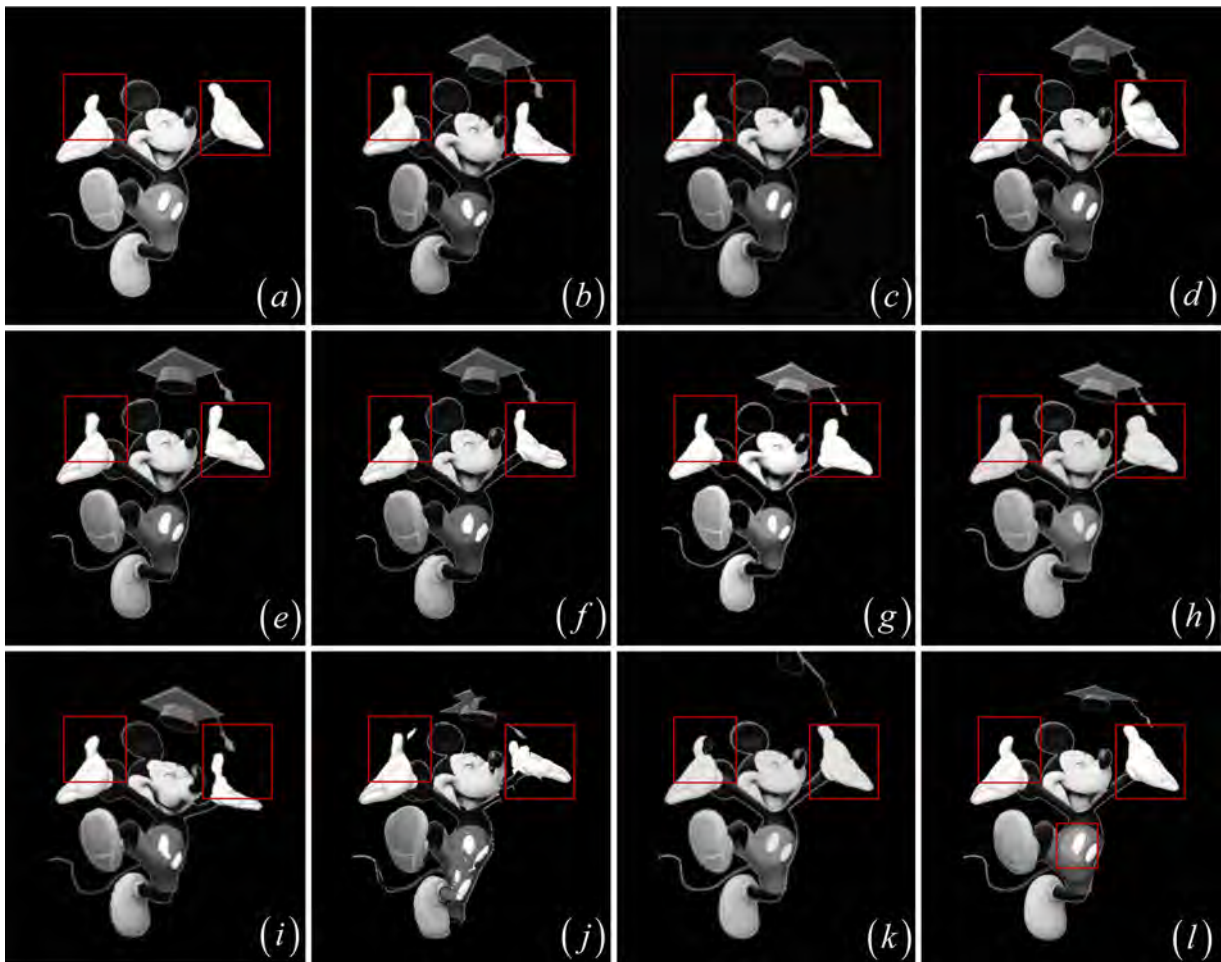


**Fig. 11.** Mickey image registration. The proposed and FVNI methods outperform the other methods. (a) and (b) The reference and moving images, (c) ours, (d) AGS1, (e) AGS2, (f) AMI, (g) DDD, (h) BMI, (i) AMM, (j) EPPM, (k) LDOF, (l) FVNI. (For interpretation of the references to color in text, the reader is referred to the web version of the article.)

correspondences into the tumor region of the post-operative image but also incurs local large deformations that are caused by brain shift after tumor resection. A successful registered result of this case should smoothly deform the tumor region and surrounding pre-operative brain tissues (see the red boxes in Fig. 12) according to the post-operative image structures regardless of tumor resection. Visual inspection has revealed that the proposed and AMI methods (see Fig. 12(c) and (f)) apparently perform better than other methods. Because of the missing correspondences and local brain deformations in the tumor resection region, the intensity-based driving force along with the highly flexible deformation model in the AGS1, AGS2, FVNI (Fig. 12(d) and (e), (l)) methods have introduced an excessive deformation diffusion within tumor region and some non-smooth distortions across the tumor region boundaries (see the red boxes in Fig. 12(d) and (e), (l)). Meanwhile, the DDD, AMM and LDOF methods (Fig. 12(g), (i) and (k)) produce insufficient contraction of tumor region while the high degree of freedom allowed by B-spline based free-form deformation in BMI method (Fig. 12(h)) has introduced an excessive shrinkage of the tumor regions. The EPPM (Fig. 12(j)) method obtains a big hole in normal brain tissue and bad topology changes within and around the tumor resection region. This visual valuation is further confirmed by landmark-based registration evaluation in the following section, though the landmark-based evaluation cannot fully reflect each method's real performance due to its incapability in defining

the corresponding landmark pairs within and around the tumor resection region.

A more challenging flower image registration is displayed in Fig. 13, where the small scale stamen filament in the right part of the image is largely deformed while some buds behind the stamen filament of the moving image are disappeared in the reference image (see the top red boxes in Fig. 13). Accurately matching small scale structures that have large deformations and missing correspondences is very difficult for nonrigid image registration and becomes the touchstone of an excellent structure matching method. Therefore, an ideal registration algorithm must accurately match not only the large petal (see the bottom red boxes) but also the small stamen filament while simultaneously keeping reasonable local deformation consistency in the spatial context. Among the 10 methods, only the proposed (Fig. 13(c)), FVNI (Fig. 13(l)) and AMM (Fig. 13(i), with the mask definition in Fig. 10(d)) methods align not only the small scale stamen filament but also the large scale petals by computing their reasonable, smooth and accurate deformations. On the contrary, the AGS1 (Fig. 13(d)) achieves excessive and non-smooth deformations in the small scale stamen filament and large scale petals such that the stamen filament is crooked and a few edge parts of the petals are twisted and cocked up. These excessive deformations in the stamen filament and petals are also more or less visible in the registered results from the AGS2 (Fig. 13(e)) and AMM (Fig. 13(i)) methods. The LDOF (Fig. 13(k)) method

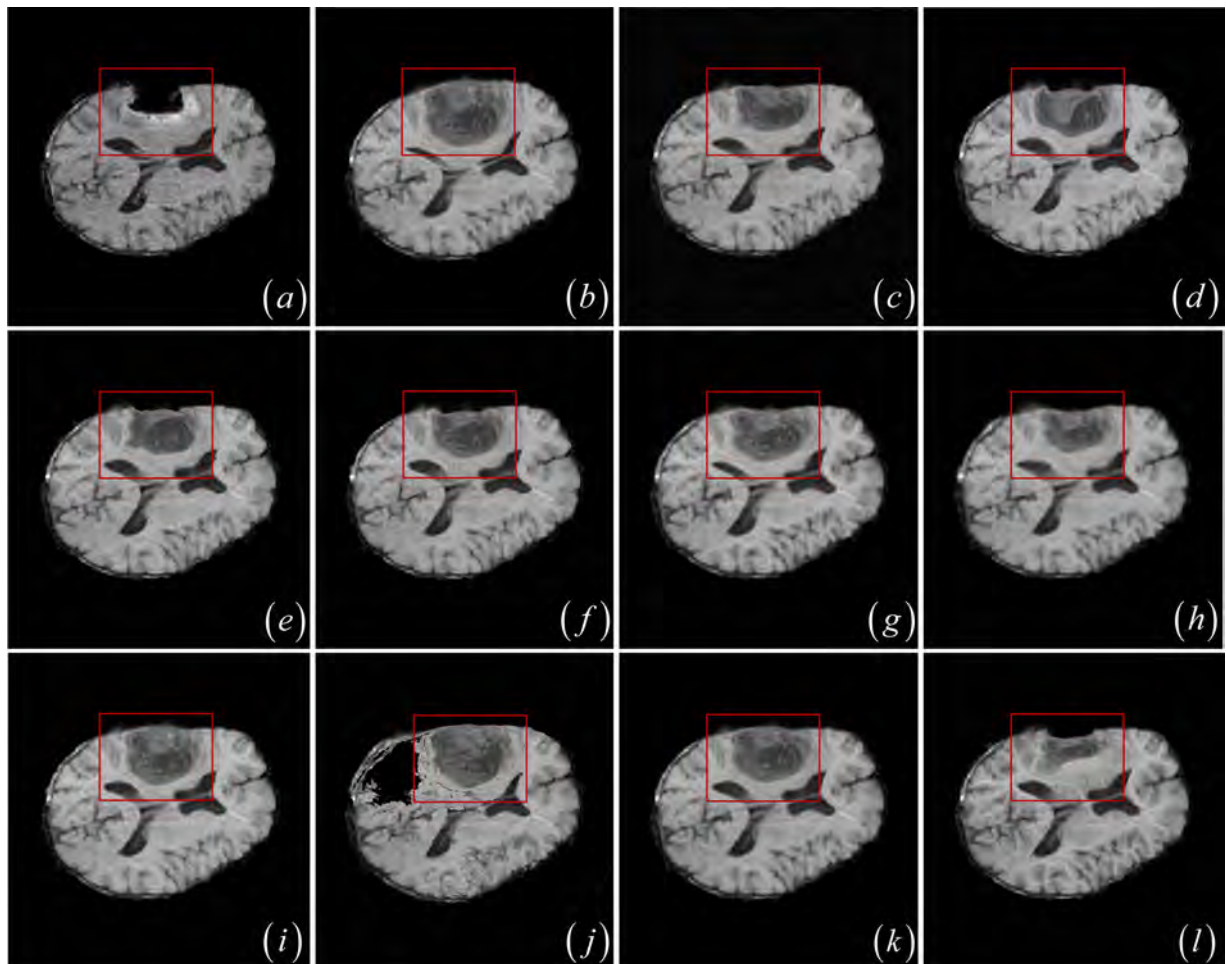


**Fig. 12.** Brain tumor image registration. The proposed and AMI methods outperform other methods. (a) and (b) The reference and moving images, (c) ours, (d) AGS1, (e) AGS2, (f) AMI, (g) DDD, (h) BMI, (i) AMM, (j) EPPM, (k) LDOF, (l) FVNI. (For interpretation of the references to color in text, the reader is referred to the web version of the article.)

gets better deformations for most structures than the DDD and BMI methods (Fig. 13(g) and (h)), but also apparently introduces some artifacts in the petals of the registered moving image. The EPPM method (Fig. 13(j)) still produces bad topology change in the petals.

The MREs and SDs of the manually selected landmark pairs (Fig. 10(e)–(g)) for the 10 methods in the three grayscale image registration are listed in Table 1. Because the EPPM method produced topology changes and complex artifacts in all three experiments such that we cannot find the corresponding landmarks in the deformed moving image, EPPM's registration errors are unavailable in Table 1. The proposed and FVNI methods for the Mickey image matching achieve the smallest and second smallest registration errors of  $1.27 \pm 3.09$  and  $1.76 \pm 2.96$  pixels, respectively, while the registration errors of AGS1, AGS2, AMI, DDD, BMI, AMM, and LDOF methods are greater than or equal to  $1.87 \pm 3.11$  pixels. These landmark-based evaluation results are consistent with the above-mentioned visual evaluation results.

As for the brain images, the missing correspondences resulted from brain tumor resection prevent sufficient corresponding landmark definitions (Fig. 10(f)) in the tumor resection region. Based on the salient corresponding landmark pairs in the normal tissues, we find that the proposed, AGS2, AMI and FVNI methods have achieved sub-pixel registration accuracy with the registration errors of  $0.97 \pm 1.91$ ,  $0.83 \pm 0.61$ ,  $0.95 \pm 1.48$  and  $0.81 \pm 0.70$  pixels, respectively. Due to the landmark definition incapability in the

tumor resection region, the lowest and second lowest landmark-based registration errors achieved by FVNI and AGS2 methods do not reflect these two methods' unacceptable deformation diffusion and non-smooth edge structure distortions in the tumor region and its boundary. However, these normal structure based registration errors provided by the FVNI and AGS2 suggest that these two excellent methods' perfect performances in matching normal structures in brain images. As for the flower image, the proposed and FVNI methods get the smallest and second smallest registration errors of  $1.14 \pm 2.96$  and  $1.21 \pm 1.69$  pixels, respectively, while the registration errors of other methods are greater than or equal to  $1.55 \pm 3.49$  pixels.

In average, the proposed method obtains almost the best performance in comparison with other methods for matching all these challenging structures with outliers. Although the AMI method in the brain tumor resection image registration has a slight advantage over the proposed method, this advantage is mainly due to the contributions from the high accuracies in matching normal structures allowed by AMI method. The proposed method achieves the excellent performance in matching all outlier structures from visual inspection, but the missing correspondences of landmarks in these outlier structures limit the landmark-based evaluation in reflecting the overall performances of the proposed and the other methods.

Besides our method, AGS2, FVNI and AMI have achieved better performances than other state-of-art methods in a few cases of matching Chinese character and three challenging outlier

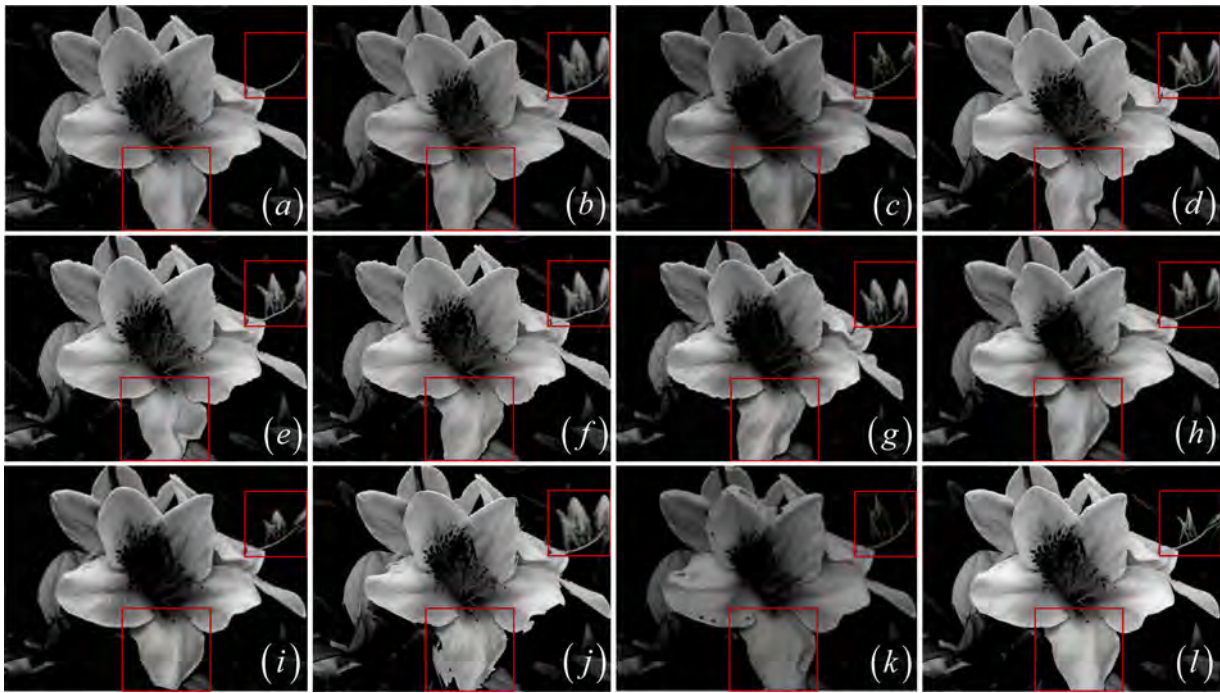


**Fig. 13.** Flower image registration. The proposed, FVNI and AMM methods perform better than other methods. (a) and (b) The reference and moving images, (c) ours, (d) AGS1, (e) AGS2, (f) AMI, (g) DDD, (h) BMI, (i) AMM, (j) EPPM, (k) LDOF, (l) FVNI. (For interpretation of the references to color in text, the reader is referred to the web version of the article.)

structures. We try to analyze several factors that lead to the success of these four methods as follows: first, due to the transformation model with the similarity measure and the optimization strategy being three important components of nonrigid image registration, the high degree of freedom allowed by a deformation mechanism, such as the most flexible deformation model by defining a displacement vector to each pixel as used in our method and FVNI, the large deformation diffeomorphic metric matching (LDDMM) model as used in AGS1 and AGS2 and the B-spline based free from deformation (FFD) model as used in BMI, is assumed to be an important factor contributing to the high registration accuracy in matching challenging structures. However, the high degree of freedom in LDDMM model for AGS1 and AGS2 and FFD model for BMI method also can result in excessive deformations at our experiments because the global intensity-based energy minimization optimization can easily mislead the outlier structure matching. Second, the symmetric diffeomorphic setting in AGS2 and FVNI also contributes to the accuracy and robustness in outlier structure matching. The proposed method adopts one pixel displacement in each level of multi-resolution block matching to guarantee diffeomorphism condition. Generally, these diffeomorphic approaches prevent singularities from arising in the displacement field. A proper transformation model, which is of sufficient degrees of freedom but well regularized by the diffeomorphism or even the symmetric diffeomorphism design with regard to the two images, is the first choice for challenging outlier structure matching.

Third, the symmetric normalization feature as introduced in AGS2 has seemed to at least partly contribute to its accuracy and robustness in matching Chinese character. Specifically, in the binary structure matching with missing correspondences and local large deformations, where two binary images have obvious intensity contrast between the white Chinese character and black background, AGS2 has best accuracies in matching the normal regions (the lower left stroke in Fig. 8(e)) and in the immediately neighboring abnormal regions. This is perhaps due to the symmetric normalization setting, which deforms both images to “hidden middle template” between the two images. That is, a difficult problem of minimizing the full distance (dissimilarity measure) between the two challenging images is decoupled into two relatively simpler subproblems that minimize the half distances between either image and the hidden middle template. Fourth, the same non-parametric variational scheme, which defines the registration problem as finding a parametrizing velocity fields within multi-resolution gradient descent optimization, implemented in AGS2, FVNI and AMI can be an advantageous factors for these methods’ success in matching challenging structures. Future research should explore in detail the advantage of this non-parametric variational registration scheme for the challenging structure matching with outliers.

At last, the outlier structures with both missing correspondences and local large deformations introduce significant challenges for the state-of-art nonrigid image registration.

**Table 1**

Registration errors (Mean + SD) of the 10 methods for the three grayscale image registrations. Due to the landmarks’ missing correspondences in the outlier structures, only the boldface registration errors represent the real excellent performance metrics that are in complete agreement with the visual evaluation.

Method	Mickey	Brain	Flower	Method	Mickey	Brain	Flower
Ours	<b>1.27 ± 3.09</b>	<b>0.97 ± 1.91</b>	<b>1.14 ± 2.96</b>	BMI	3.23 ± 5.51	1.15 ± 1.89	4.42 ± 5.65
AGS1	1.87 ± 3.11	1.04 ± 0.89	3.24 ± 3.85	AMM	12.03 ± 14.80	1.16 ± 1.99	1.55 ± 3.49
AGS2	1.98 ± 3.32	0.83 ± 0.61	1.77 ± 3.42	EPPM	–	–	–
AMI	2.35 ± 3.79	<b>0.95 ± 1.48</b>	2.4 ± 3.4	LDOF	3.55 ± 3.21	1.97 ± 1.93	2.72 ± 2.35
DDD	6.07 ± 5.93	1.60 ± 3.08	8.38 ± 8.82	FVNI	<b>1.76 ± 2.96</b>	0.81 ± 0.70	<b>1.21 ± 1.69</b>

**Table 2**

Computation runtime in seconds for the 10 registration methods (Inter(R) Core(TM) i5-4460 Quad-Core 3.2 GHz CPU, RAM 4.0 GB).

Cases	Ours	AGS1	AGS2	AMI	DDD	BMI	AMM	EPPM	LDOF	FVNI
1	17.67	3563	30.67	13.99	4.42	11.41	13.99	0.79	41.23	4.02
2	18.83	3521.5	54.64	21.52	4.99	16.14	17.29	0.90	55	2.99
3	35.86	3761.5	33.88	15.69	8.97	32	14.94	0.90	84.43	4.53
4	14.67	3271.3	26.16	8.56	4.08	30.57	2.85	0.74	68.48	2.82

Presently, the state-of-art nonrigid registration methods do not explore the consistencies which exist in the normal structures and their local deformations surrounding the outlier regions. For example, simply excluding the outlier structures in minimization of cost function between the images by AMM's cost function masking strategy is not enough to accurately match local saliency structures with missing correspondences and local large deformations. However, the structures and their deformations' consistencies are fully explored by kernel regression of local deformation fields in the proposed method to boost the structure matching performance.

Table 2 lists the computation time needed for the 10 algorithms at the four image registrations, where the image resolution of case 1–3 is  $372 \times 392$  pixels, and that of case 4 is  $384 \times 288$  pixels. All the 10 methods are operated on a PC of Intel Core i5-4460 Quad-Core 3.2 GHz CPU with 4 GB memory.

#### 4. Conclusion and discussion

In this paper, we compute saliency map of each image based on the dissimilarity between neighboring local structure tensors to indicate the local saliency structure distribution, and propose new JSM to describe the matching degree between the two saliency maps at every pixel pair in the overlapping regions of the two images. The JSM guides the local adaptive kernel regression for the dense deformation field reconstruction in accurately matching local structures while suppressing outlier effects in the nonrigid image registration. The proposed method also makes the regression kernel not only locally adaptive to the JSSs in the two images but also to reference image's saliency structures. These strategies enhance the proposed algorithm in achieving the accuracy and robustness of structure matching with missing correspondences and local large deformations.

Nevertheless, there are still some issues that need to be further addressed in our future work. Firstly, the local scale of regression kernel in Section 2.3 is set as a constant value (1.5) for the sake of simplicity at each anisotropic Gaussian kernel. As shown in some registered results, however, the deformations of some small scale structures (such as the eyes in the doll image at Fig. 7) are affected somewhat badly by the deformations of the surrounding large scale structures. This situation is caused by the unchangeable local scales. Indeed, the local scale (the width of kernel) controls the number of discrete displacement vectors contributing to the reconstruction of dense deformation vectors. Therefore, the choice of local scale significantly affects the final registration result. A self-adjustable local scale according to the local structure properties is expected to automatically adjust the number of discrete displacement vectors participating in the deformation reconstruction. To the best of our knowledge, almost no attention has been paid on the self-adjustable local scale for nonrigid image registration during the last decade.

Secondly, as for the symmetric diffeomorphism of nonrigid image registration [45,48], the missing correspondences and local large deformations make it unrealistic for nonrigid registration method enforcing the symmetric diffeomorphic local structure matching. Meanwhile, our current work uses the full information from reference image's structure to guide the anisotropic kernel design in kernel regression, which prevents the symmetric

diffeomorphic registration strategy in our work. However, symmetry is desired for estimating the distance between reference and moving structures in the two images and makes results independent of arbitrary decisions about which image is "reference" or "moving". However, we can initialize our method with some symmetric diffeomorphic registration algorithms to find the local structure's optimal symmetric diffeomorphic matching for the subsequent JSS adaptive kernel regression.

At last, further experimental researches are required to give thorough tests on 3D structure matching. At present, the objective and rigorous evaluation of 3D structure matching performance was hampered by the absence of public appropriate reference standard 3D image data sets. Though there are two public 3D image data DIR-Lab [50]<sup>10</sup> and POPI [51],<sup>11</sup> both of them cannot meet the following two challenges. The desired reference 3D image data to test 3D structure matching should reflect the two major challenges: (1) presenting the outlier structures with both missing correspondences and local large deformations; (2) having expert-defined corresponding structural landmarks in these image data sets, with repeat structure matching performed by multiple observers to estimate the spatial variance in feature identification.

#### Acknowledgments

This work was supported by the National Natural Science Foundation of China (61271320 and 60872102). The authors would like to thank Eduardo Suarez, Rafael Nebot for creating the block matching framework and all authors for opening source codes used in the experimental comparison in this work. The authors thank the open source ANTs project, MIPAV, Diffeomorphic Demons, 3D Slicer and ITK (<http://www.itk.org/>) project. The authors would like to thank Zeshan Fu for his evaluation work. We are thankful to the anonymous reviewers for their valuable comments that greatly helped to improve this paper.

#### References

- [1] A. Sotiras, C. Davatzikos, N. Paragios, Deformable image registration: a survey, *IEEE Trans. Med. Imag.* 32 (7) (2013) 1153–1190.
- [2] T. Brox, J. Malik, Large displacement optical flow: descriptor matching in variational motion estimation, *IEEE Trans. Pattern Anal. Mach. Intel.* 33 (3) (2011) 500–513.
- [3] H. Chui, A. Rangarajan, A new point matching algorithm for non-rigid registration, *Comput. Vis. Image Underst.* 89 (2–3) (2003) 114–141.
- [4] Y. Zheng, E. Daniel, A.A. Hunter III, R. Xiao, J. Gao, H. Li, M.G. Maguire, D.H. Brainard, J.C. Gee, Landmark matching based retinal image alignment by enforcing sparsity in correspondence matrix, *Med. Image Anal.* 18 (2014) 903–913.
- [5] X. Yang, J. Pei, J. Shi, Inverse consistent non-rigid image registration based on robust point set matching, *Biomed. Eng. Online* 13 (Suppl 2) (2014) S2.
- [6] A. Myronenko, X. Song, Point set registration: coherent point drift, *IEEE Trans. Pattern Anal. Mach. Intell.* 32 (2010) 2262–2275.
- [7] S. Sousa, W.G. Kropatsch, Graph-based point drift: graph centrality on the registration of point-sets, *Pattern Recognit.* 48 (2015) 368–379.
- [8] Q. Sang, J. Zhang, Z. Yu, Robust non-rigid point registration based on feature-dependant finite mixture model, *Pattern Recognit. Lett.* 34 (2013) 1557–1565.
- [9] Y. Ou, C. Davatzikos, DRAMMS: Deformable Registration Via Attribute Matching and Mutual-Saliency Weighting, *IPMI 2009 LNCS*, vol. 5636, 2009, pp. 50–62.

<sup>10</sup> <http://www.dir-lab.com/>

<sup>11</sup> <http://www.creatis.insa-lyon.fr/rio/popi-model/>

- [10] S. Periaswamy, H. Farid, Medical image registration with partial data, *Med. Image Anal.* 10 (2006) 452–464.
- [11] J. Ma, J.C.W. Chan, F. Canters, An operational superresolution approach for multi-temporal and multi-angle remotely sensed imagery, *IEEE J. Sel. Top. Appl. Earth Obs. Remote Sens.* 5 (2012) 110–124.
- [12] B. Yeo, M. Sabuncu, R. Desikan, B. Fischl, P. Golland, Effects of registration regularization and atlas sharpness on segmentation accuracy, *Med. Image Anal.* 12 (2008) 603–615.
- [13] R. Stefanescu, O. Commowick, G. Malandain, P.-Y. Bondiau, N. Ayache, X. Pennec, Non-Rigid Atlas to Subject Registration with Pathologies for Conformal Brain Radiotherapy, *MICCAI 2004 LNCS*, vol. 3216, 2004, pp. 704–711.
- [14] F.F. Berendsen, A.N.T.J. Kotte, A.A.C. de Leeuw, I.M. Jurgenliemk-Schulz, M.A. Viergever, J.P.W. Pluim, Registration of structurally dissimilar images in MRI-based brachytherapy, *Phys. Med. Biol.* 59 (2014) 4033–4045.
- [15] P. Risholm, E. Samset, I. Talos, W. Wells, A Non-Rigid Registration Framework that Accommodates Resection and Retraction, *IPMI 2009 LNCS*, vol. 5636, 2009, pp. 447–458.
- [16] L. Tang, G. Hamarneh, R. Abugharbieh, Reliability-Driven, Spatially-Adaptive Regularization for Deformable Registration, *WBIR 2010 LNCS*, vol. 6204, 2010, pp. 173–185.
- [17] N. Chitphakdithai, K.P. Vives, J.S. Duncan, Registration of Brain Resection MRI with Intensity and Location Priors, in: 2011 IEEE International Symposium on Biomedical Imaging: From Nano to Macro, 2011, pp. 1520–1523.
- [18] I.J.A. Simpson, J.A. Schnabel, A.R. Groves, J.L.R. Andersson, M.W. Woolrich, Probabilistic inference of regularisation in non-rigid registration, *NeuroImage* 59 (2012) 2438–2451.
- [19] M. Foskey, B. Davis, L. Goyal, S. Chang, E. Chaney, N. Strehl, S. Tomei, J. Rosenman, S. Joshi, Large deformation 3D image registration in image-guided radiation therapy, *Phys. Med. Biol.* 50 (24) (2005) 5869–5892.
- [20] S. Gao, L. Zhang, H. Wang, R. de Crevoisier, D.D. Kuban, R. Mohan, L. Dong, A deformable image registration method to handle distended rectums in prostate cancer radiotherapy, *Med. Phys.* 33 (9) (2006) 3304–3312.
- [21] M. Bach Cuadra, M. De Craene, V. Duay, B. Macq, C. Pollo, J.-Ph. Thiran, Dense deformation field estimation for atlas-based segmentation of pathological MR brain images, *Comput. Methods Programs Biomed.* 84 (2006) 66–75.
- [22] E.I. Zacharakis, C.S. Hogeia, D. Shen, G. Biros, C. Davatzikos, Non-diffeomorphic registration of brain tumor images by simulating tissue loss and tumor growth, *NeuroImage* 46 (2009) 762–774.
- [23] A. Mang, S. Becker, A. Toma, T. Buzug, Coupling tumor growth with brain deformation: a constrained parametric non-rigid registration problem, in: *Medical Imaging 2010: Image Processing*, Proc. SPIE 7623 (2010), 76230C-1–12.
- [24] M. Sdika, D. Pelletier, Nonrigid registration of multiple sclerosis brain images using lesion inpainting for morphometry or lesion mapping, *Hum. Brain Mapp.* 30 (4) (2009) 1060–1067.
- [25] M. Brett, A.P. Leff, C. Rorden, J. Ashburner, Spatial normalization of brain images with focal lesion using cost function masking, *NeuroImage* 14 (2) (2001) 486–500.
- [26] S.M. Andersen, S.Z. Rapcsak, P.M. Beeson, Cost function masking during normalization of brains with focal lesions: still a necessity, *NeuroImage* 53 (1) (2010) 78–84.
- [27] P. Ripolles, J. Marco-Pallares, R. de Diego-Balaguer, J. Miro, M. Falip, M. Juncadella, F. Rubio, A. Rodriguez-Fornells, Analysis of automated methods for spatial normalization of lesioned brains, *NeuroImage* 60 (2) (2012) 1296–1306.
- [28] V. Katkovnik, A. Foi, K. Egiazarian, J. Astola, From local kernel to nonlocal multiple-model image denoising, *Int. J. Comput. Vis.* 86 (1) (2010) 1–32.
- [29] P. Milanfar, A tour of modern image filtering: new insights and methods, both practical and theoretical, *IEEE Signal Process. Mag.* 30 (1) (2013) 106–128.
- [30] E. Suarez, C.-F. Westin, E. Rovaris, J. Ruiz-Alzola, Nonrigid Registration Using Regularized Matching Weighted by Local Structure, *MICCAI 2002 LNCS*, vol. 2489, 2002, pp. 581–589.
- [31] R. Gallea, E. Ardiczone, R. Pirrone, O. Gambino, Three-dimensional fuzzy kernel regression framework for registration of medical volume data, *Pattern Recognit.* 46 (11) (2013) 3000–3016.
- [32] B.W. Papiiez, M.P. Heinrich, J. Fehrenbach, L. Risser, J.A. Schnabel, An implicit sliding-motion preserving regularisation via bilateral filtering for deformable image registration, *Med. Image Anal.* 18 (2014) 1299–1311.
- [33] D. Demirovic, A. Serifovic-Trbalic, W. Prljaca, Ph.C. Cattin, Bilateral filter regularized accelerated Demons for improved discontinuity preserving registration, *Comput. Med. Imag. Graph.* 40 (2015) 94–99.
- [34] W. Cho, A. Koschan, M.A. Abidi, Fundamental relationship between bilateral kernel and locally adaptive regression kernel, *Electron. Lett.* 49 (2013) 335–337.
- [35] B. Qin, Z. Gu, X. Sun, Y. Lv, Registration of images with outliers using joint saliency map, *IEEE Signal Process. Lett.* 17 (1) (2010) 91–94.
- [36] Z. Gu, B. Qin, Nonrigid registration of brain tumor resection MR images based on joint saliency map and keypoint clustering, *Sensors* 9 (12) (2009) 10270–10290.
- [37] A. Rodriguez, C. Fernandez-Lozano, J. Dorado, J.R. Rabunal, Two-dimensional gel electrophoresis image registration using block-matching techniques and deformation models, *Anal. Biochem.* 454 (2014) 53–59.
- [38] J. Zhou, B. Qin, Geometrical regularization of nonrigid registration using local anisotropic structure and joint saliency map, in: *Proc. SPIE 8009, Third International Conference on Digital Image Processing (ICDIP 2011)*, 800913, July 08 2011.
- [39] P. Rogelj, S. Kovacic, J.C. Gee, Point similarity measures for non-rigid registration of multi-modal data, *Comput. Vis. Image Underst.* 92 (2003) 112–140.
- [40] T.Q. Pham, L.J. van Vliet, K. Schutte, Robust fusion of irregularly sampled data using adaptive normalized convolution, in: *EURASIP J. APPL. SIG. Proc.* 2006, pp. 1–12.
- [41] H. Takeda, S. Farsiu, P. Milanfar, Kernel regression for image processing and reconstruction, *IEEE Trans. Image Proc.* 16 (2) (2007) 349–366.
- [42] C.F. Westin, *A Tensor Framework for Multidimensional Signal Processing*, Ph.D. Thesis, Linköping University, Sweden, 1994.
- [43] A. Borji, L. Itti, State-of-the-art in visual attention modeling, *IEEE Trans. Pattern. Anal. Mach. Intell.* 35 (1) (2013) 185–207.
- [44] H. Zhang, P.A. Yushkevich, D.C. Alexander, J.C. Gee, Deformable registration of diffusion tensor MR images with explicit orientation optimization, *Med. Image Anal.* 10 (5) (2006) 764–785.
- [45] B.B. Avants, N.J. Tustison, G. Song, P.A. Cook, A. Klein, J.C. Gee, A reproducible evaluation of ANTs similarity metric performance in brain image registration, *NeuroImage* 54 (3) (2011) 2033–2044.
- [46] T. Vercauteren, X. Pennec, A. Perchant, N. Ayache, Diffeomorphic demons: efficient non-parametric image registration, *NeuroImage* 45 (2009) S61–S72.
- [47] L. Bao, Q. Yang, H. Ji, Fast edge-preserving patchmatch for large displacement optical flow, *IEEE Trans. Image Proc.* 23 (12) (2014) 4996–5006.
- [48] R. Werner, A. Schmidt-Richberg, H. Handels, J. Ehrhardt, Estimation of lung motion fields in 4D CT data by variational non-linear intensity-based registration: a comparison and evaluation study, *Phys. Med. Biol.* 59 (2014) 4247–4260.
- [49] T. Rohlfing, Image similarity and tissue overlaps as surrogates for image registration accuracy: widely used but unreliable, *IEEE Trans. Med. Imag.* 31 (2) (2012) 153–163.
- [50] R. Castillo, E. Castillo, R. Guerra, V.E. Johnson, T. McPhail, A.K. Garg, T. Guerrero, A framework for evaluation of deformable image registration spatial accuracy using large landmark point sets, *Phys. Med. Biol.* 54 (2009) 1849–1870.
- [51] J. Vandemeulebroucke, S. Rit, J. Kybic, P. Clarysse, D. Sarrut, Spatiotemporal motion estimation for respiratory-correlated imaging of the lungs, *Med. Phys.* 38 (1) (2011) 166–178.